

Energetic ions in ITER plasmas

Cite as: Phys. Plasmas **22**, 021807 (2015); <https://doi.org/10.1063/1.4908551>

Submitted: 10 October 2014 • Accepted: 21 January 2015 • Published Online: 13 February 2015

 S. D. Pinches, I. T. Chapman, Ph. W. Lauber, et al.



[View Online](#)



[Export Citation](#)



[CrossMark](#)

ARTICLES YOU MAY BE INTERESTED IN

Mechanisms of energetic-particle transport in magnetically confined plasmas

Physics of Plasmas **27**, 030901 (2020); <https://doi.org/10.1063/1.5136237>

Basic physics of Alfvén instabilities driven by energetic particles in toroidally confined plasmas

Physics of Plasmas **15**, 055501 (2008); <https://doi.org/10.1063/1.2838239>

Physics and applications of three-ion ICRF scenarios for fusion research

Physics of Plasmas **28**, 020501 (2021); <https://doi.org/10.1063/5.0021818>



Physics of Plasmas Physics of Fluids

Special Topic: Turbulence in Plasmas and Fluids

Submit Today!

Energetic ions in ITER plasmas

S. D. Pinches,¹ I. T. Chapman,² Ph. W. Lauber,³ H. J. C. Oliver,^{4,2} S. E. Sharapov,² K. Shinohara,⁵ and K. Tani⁶

¹ITER Organization, Route de Vinon-sur-Verdon, CS 90 046, 13067 St Paul-lez-Durance Cedex, France

²CCFE, Culham Science Centre, Abingdon, Oxfordshire OX14 3DB, United Kingdom

³Max-Planck-Institut für Plasmaphysik, EURATOM-Association, Boltzmanstraße 2, D-85748 Garching, Germany

⁴H H Wills Physics Laboratory, University of Bristol, Royal Fort, Tyndall Avenue, Bristol BS8 1TL, United Kingdom

⁵Japan Atomic Energy Agency, Naka, Ibaraki 311-0193, Japan

⁶Nippon Advanced Technology Co., Ltd, Naka, Ibaraki 311-0102, Japan

(Received 10 October 2014; accepted 21 January 2015; published online 13 February 2015)

This paper discusses the behaviour and consequences of the expected populations of energetic ions in ITER plasmas. It begins with a careful analytic and numerical consideration of the stability of Alfvén Eigenmodes in the ITER 15 MA baseline scenario. The stability threshold is determined by balancing the energetic ion drive against the dominant damping mechanisms and it is found that only in the outer half of the plasma ($r/a > 0.5$) can the fast ions overcome the thermal ion Landau damping. This is in spite of the reduced numbers of alpha-particles and beam ions in this region but means that any Alfvén Eigenmode-induced redistribution is not expected to influence the fusion burn process. The influence of energetic ions upon the main global MHD phenomena expected in ITER's primary operating scenarios, including sawteeth, neoclassical tearing modes and Resistive Wall Modes, is also reviewed. Fast ion losses due to the non-axisymmetric fields arising from the finite number of toroidal field coils, the inclusion of ferromagnetic inserts, the presence of test blanket modules containing ferromagnetic material, and the fields created by the Edge Localised Mode (ELM) control coils in ITER are discussed. The greatest losses and associated heat loads onto the plasma facing components arise due to the use of the ELM control coils and come from neutral beam ions that are ionised in the plasma edge. [<http://dx.doi.org/10.1063/1.4908551>]

I. INTRODUCTION

The creation of burning plasmas in ITER will be the start of a challenging new field of physics research that requires the understanding of many fundamental issues associated with the presence of super-Alfvénic fusion-born alpha-particles.^{1,2} Present-day experiments using Neutral Beam Injection (NBI) and ion cyclotron resonance heating (ICRH) auxiliary heating systems have revealed a rich family of fast ion-driven Alfvén instabilities that are excited over a broad frequency range. The consequences on fast ion transport and confinement range from negligible in the case of benign mode saturation, to significant for high-amplitude bursting modes (see, for example, Ref. 3 and references therein). Significant progress has been made in the understanding of Alfvén instabilities,⁴ particularly in terms of the theoretical interpretation of experimental observations from many different devices. However, the scales that arise in ITER plasmas, with many modes expected and a small ratio between the passing fast particle orbit width and the minor radius, $\rho_\alpha/a \cong 10^{-2}$, goes well beyond those found in present-day experiments. For this reason, extrapolation towards ITER is not straightforward and Alfvén instability remains a significant issue for high- Q operation. Since ITER can only tolerate fast particle losses of a few percent, primarily due to the associated first wall power fluxes that they lead to, it is essential that any burning plasma experiment has a

window of operation where either the fast ion-driven Alfvén modes are stable, or, if unstable, the effect of instability leads only to a mild rearrangement of the fast-particle distribution.

In addition to the direct excitation of fast ion driven modes, energetic particles may also influence the stability of other plasma modes with further consequences for the fusion performance. A particular example is the sawtooth instability whose duration and magnitude can be affected by the population of fast ions present. Fast ions can stabilise the internal $n = 1$ kink leading to longer sawtooth cycles and larger sawtooth crashes that can trigger neoclassical tearing modes (NTMs), which then degrade the plasma confinement, including that of the fast ions.^{5–7} In high-beta scenarios operating above the no-wall beta-limit, the stability of the external $n = 1$ kink mode depends upon the resistivity of the surrounding walls as well as kinetic effects, including those from fast ions. Understanding the stability of such Resistive Wall Modes (RWMs), including the influence of energetic ions, will be important for the development of control methods and the attainment of steady-state scenarios in ITER.

Aside from the self-generated imperfections in the otherwise axisymmetric confining magnetic field configuration due to the various modes and instabilities discussed above, one of the techniques envisaged for the control of Edge Localised Modes (ELMs) in ITER is the application of 3D magnetic fields, which will itself have an influence upon

energetic ion confinement. Whilst such ELM control methods are operationally important for exploiting H-mode confinement properties whilst simultaneously ensuring an appropriate lifetime of the plasma facing components and expelling impurities, procedures for their use must take into account the impact on energetic ion confinement.

To support the preparation for ITER operations and the execution of the ITER Research Plan, a suite of numerical codes will be needed which can evaluate energetic ion behaviour. This includes calculating the linear stability of Alfvén Eigenmodes (AEs) in the system, as well as predicting the (nonlinear) consequences of these and other modes (including 3D equilibrium field distortions such as those due to the ELM coils) in terms of the magnitude and temporal evolution of any localised fast ion redistribution, losses, or heat loads.

This paper presents the latest developments in both theory and numerical modelling and primarily focuses upon the flat-top burning phase of an ITER 15 MA baseline scenario,⁸ which lies at the heart of ITER's primary mission, namely the delivery of a $Q = 10$ burning plasma. A 9MA steady-state scenario operating above the no-wall beta limit is also briefly considered since the interaction of energetic particles with RWMS becomes important in such cases. A detailed assessment of scenarios operating at reduced plasma currents and fields in the early non-nuclear period of operations is left for future work.

II. ITER 15MA BASELINE SCENARIO: PROFILES AND EQUILIBRIA

We consider plasma parameters and profiles predicted using the ASTRA transport code for the ITER baseline scenario^{8,9} with a plasma current $I_P = 15$ MA, $R_0 = 6.2$ m, $a = 2$ m, and $B_0 = 5.3$ T. The model is based on 2D SPIDER equilibria for this ITER plasma, and the prediction of the plasma profiles is obtained from a 1D scaling-based transport model for the electron and hydrogenic ions for the electron and ion temperatures, T_e, T_i , current density, j , electron and ion densities, $n_e, n_{DT}, n_T, n_{He}, n_{Be}$. The electron density profile is assumed to be flat due to the low core particle sources in ITER and the fuel ion species are assumed to have a deuterium-tritium (DT) mixture close to the optimum, $n_D : n_T \approx 50 : 50$, while the density of helium ions resulting from the fusion reactions varies as a function of fusion reactivity, and the beryllium impurity ions coming from the first wall is taken to be

$$n_{Be} = 0.02 n_e. \quad (1)$$

The auxiliary heating and current drive includes two deuterium negative NBI sources with $E_{beam} = 1$ MeV and an injected power of $P_{beam} = 16.5$ MW (on-axis) and 16.5 MW (off-axis). ECRH from the upper launcher is aimed in the vicinity of the $q = 3/2$ surface, with the deposited power being $P_{ECRH} = 6$ MW for the control of NTMs. This ITER plasma has a fusion gain $Q = 10$ with a total plasma heating level of 40 MW.

Figures 1–4 show the profiles of densities and temperatures of the thermal plasma, as well as the alpha-particle and

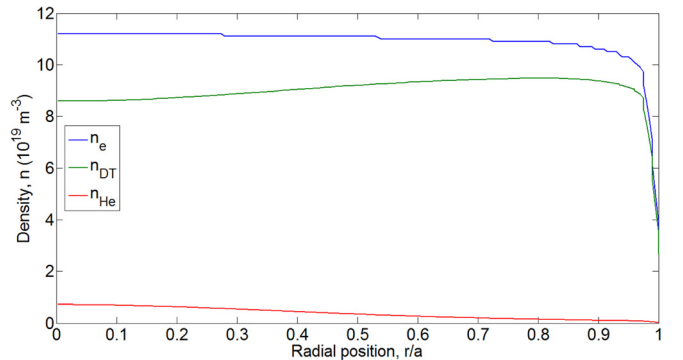


FIG. 1. Density profiles of electrons (blue), DT mixture (green), and He (red) versus normalized radius for the ITER 15 MA baseline scenario.

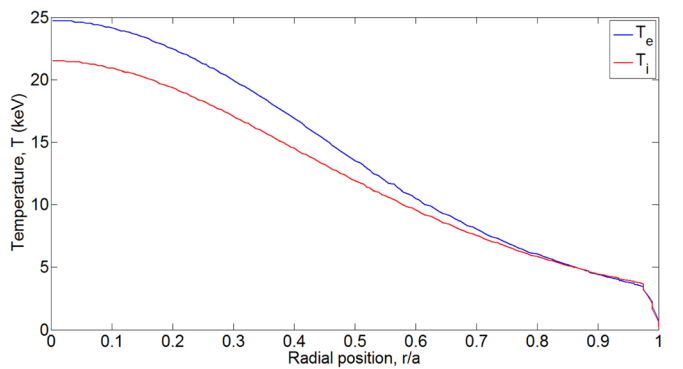


FIG. 2. Profiles of electron temperature (blue) and DT ion temperature (red) versus normalized radius.

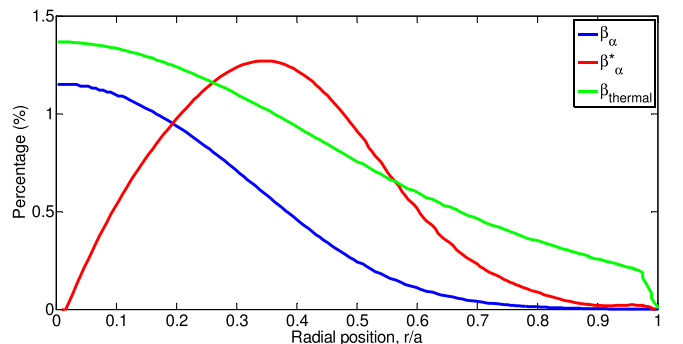


FIG. 3. Profiles of β_α (%), normalised gradient of alpha-particle pressure $\beta_\alpha^* = -ad\beta_\alpha/dr$ and thermal plasma β in the 15MA ITER baseline scenario considered versus normalized radius.

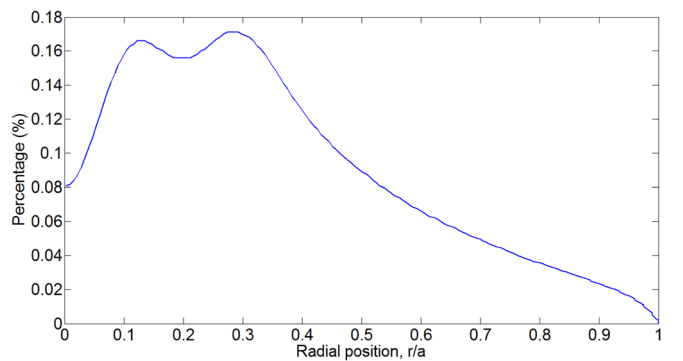


FIG. 4. Profile of β_{beam} (%) in the 15MA ITER baseline scenario considered versus normalized radius.

beam ion profiles for the $Q = 10$ operational point. The energetic alpha-particle and beam populations are computed using a Fokker-Planck approach.

It is important to note from Figure 3 that almost all of the alpha-particles are confined within the central region of the plasma, $r/a \leq 0.5$, with the highest gradient of the alpha-particle pressure at $r/a \approx 0.42$. It should also be noted that the ion temperature is quite peaked, with a central temperature $T_D(0) = T_T(0) \approx 22$ keV, and that the half-radius temperature is almost a factor of two lower, $T_D(r/a = 0.5) = T_T(r/a = 0.5) \approx 12$ keV. In contrast to the temperature, the electron density profile is very flat up to the edge region of the plasma, $r/a \approx 0.9$. The He ash profile is peaked on-axis, with the DT ion profile depleted, correspondingly, on-axis.

The baseline sawtooth scenario in ITER is expected to have a flat safety factor profile $q(r)$ in the plasma core region. For the fixed value of total current, $I_P = 15$ MA, we consider three $q(r)$ -profiles with weakly positive and weakly negative magnetic shear and on-axis values of $q(0) = 0.9$, 0.986, 1.15, as shown in Figures 5 and 6. Again, as for the alpha-particle pressure, two very different plasma regions should be noted, the low-shear core region, $r/a \leq 0.5$, and the external high-shear region, $0.5 \leq r/a \leq 1$.

III. STRUCTURE OF TOROIDICITY-INDUCED ALFVÉN EIGENMODE (TAE) AND ELLIPTICITY-INDUCED ALFVÉN EIGENMODE (EAE) GAPS, CORE-LOCALISED AND GLOBAL TAE AND EAE MODES

It is instructive to start the analysis of the Alfvén instabilities by investigating the radially localised regions of the TAEs¹⁰ and EAEs¹¹ gaps for different toroidal and poloidal mode numbers, n and m . These regions of radial localisation, r_{TAE} and r_{EAE} , are determined by the $q(r)$ -profile

$$q(r_{TAE}) = \frac{m - 1/2}{n}, \quad (2)$$

$$q(r_{EAE}) = \frac{m - 1}{n}, \quad (3)$$

with the radial width of each gap, which is also the characteristic width of the AE poloidal harmonics, given by

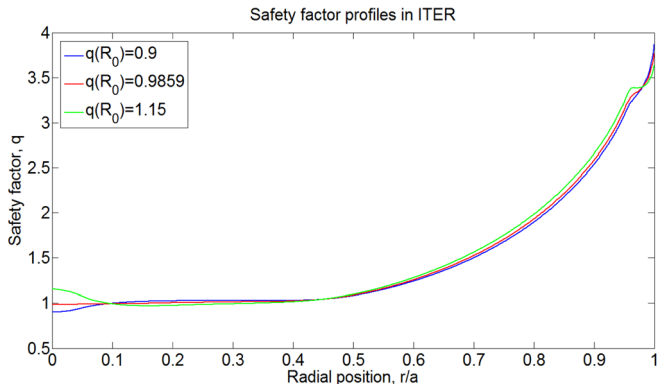


FIG. 5. $q(r)$ -profiles in the 15 MA scenario considered versus normalized radius.

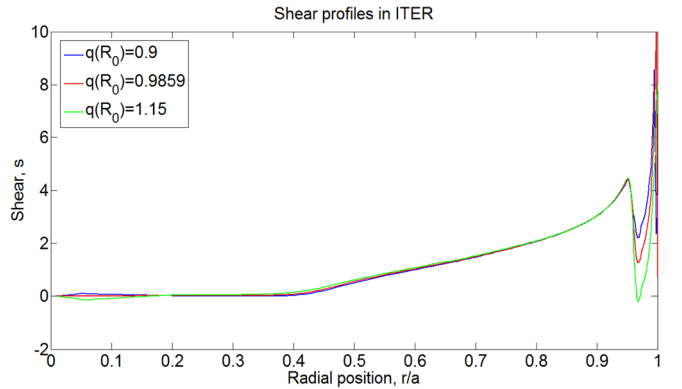


FIG. 6. Profiles of the magnetic shear in the 15 MA scenario considered versus normalized radius.

$$\Delta_{AE} \cong r_{AE}/m, \quad (4)$$

where r_{AE} is the radial localisation of the gap.

The relevant range of toroidal mode numbers to be considered for ITER is determined by the efficiency of the alpha particle drive. The maximum transfer of power between alpha-particles and an AE is achieved when the drift orbit width of a resonant passing alpha-particle, Δ_α , is comparable to the mode width, Δ_{AE} ,

$$\Delta_\alpha \cong \frac{qV_A}{\omega_{B\alpha}} \cong \Delta_{AE} \cong \frac{r_{AE}}{m} \approx \frac{r_{AE}}{nq}, \quad (5)$$

where $\omega_{B\alpha}$ is the alpha-particle cyclotron frequency. From Eq. (5), an estimate for the toroidal mode number of the most driven AE at (for example) half radius, $r_{AE} \cong a/2$, can be found to be

$$n \cong 30. \quad (6)$$

For higher mode numbers, the drive decreases as m^{-2} (Ref. 12) thus giving an order of magnitude reduction for AEs with toroidal mode numbers $n \cong 100$. Figures 7–9 show the radial localisation of the TAE gaps for the three $q(r)$ -profiles introduced above and for toroidal mode numbers in the range $1 \leq n \leq 100$.

It is seen that two distinct regions exist in Figures 7–9, with very different densities of TAE gaps. In the core-region, $r/a \leq 0.5$, where almost all of the alpha-particles reside, TAE gaps are scarce. The very existence of TAEs is problematic in this region, apart from the “bands” of TAE-gaps with 5–10 neighbouring toroidal mode numbers clearly visible at the edge of the core region, e.g., at $0.4 \leq r/a \leq 0.5$ in Figure 7. The distances between TAE-gaps in the central region are less than Δ_{AE} , so the formation of low-shear TAE (LSTAE) may be expected in this region.^{13–15} LSTAEs consist of two coupled poloidal harmonics, but there can be several eigenfrequencies per gap. The external region, $r/a > 0.5$, has a very high density of TAE gaps. In this region, the distance between the gaps is comparable to, or less than the widths of the gaps, so that different poloidal harmonics (for any fixed n) could couple and form a global radially extended TAE-mode. Figures 3 and 4 show that although not too many alpha-particles and beam ions are expected in this external

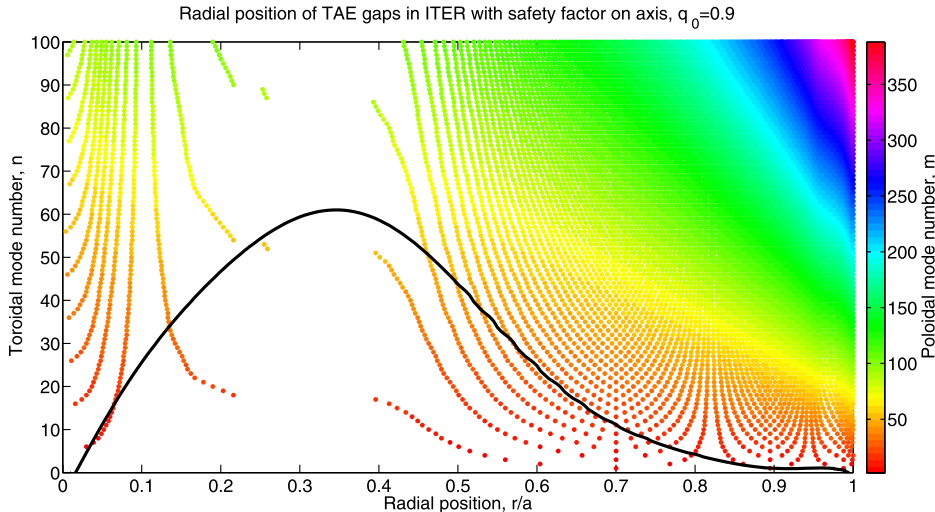


FIG. 7. Radial localisation of TAE gaps in ITER with $q_0 = 0.9$. The solid line shows the normalised radial gradient of alpha-particle pressure.

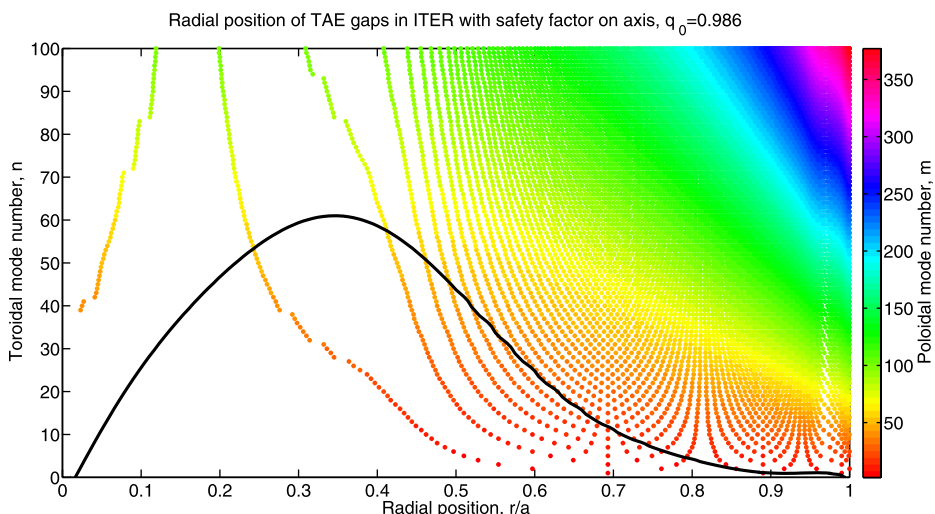


FIG. 8. Radial localisation of TAE gaps in ITER case with $q_0 = 0.986$.

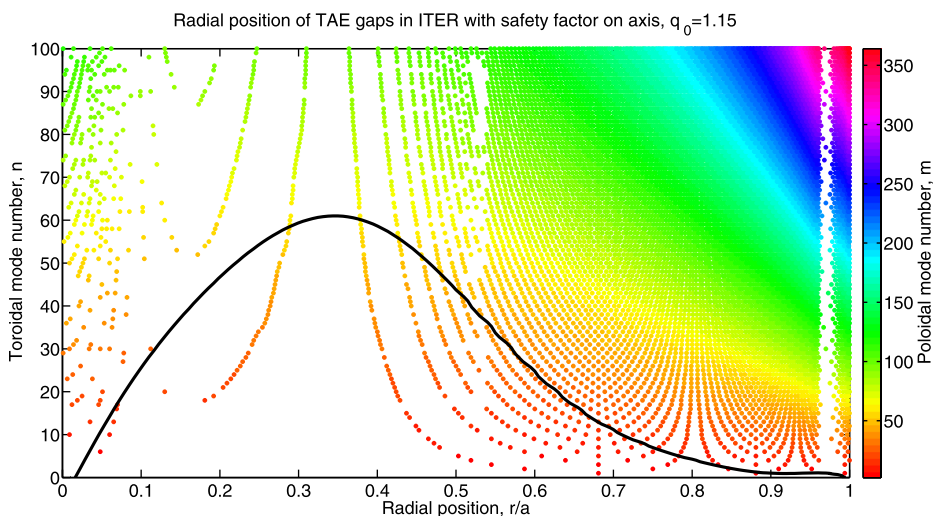


FIG. 9. Radial localisation of TAE gaps in ITER case with $q_0 = 1.15$.

region, the radial gradients of the alpha- and beam pressures available for driving Alfvén instabilities in this region are nevertheless quite high in this region.

Comparing Figure 8 to Figure 9, we see that the core region is somewhat more densely populated with TAE gaps in the case of $q(0) = 1.15$, while for the case of $q(0) = 0.9$

shown in Figure 7, there is a complete absence of TAE gaps in the region $0.25 < r/a < 0.4$.

Let us consider now some particular toroidal mode number, e.g., $n = 20$, for which Figure 7 shows the existence of a TAE-gap at $r/a \approx 0.2$ for the equilibrium with $q(0) = 0.9$. Figure 10 shows the radial structure of the $n = 20$ Alfvén

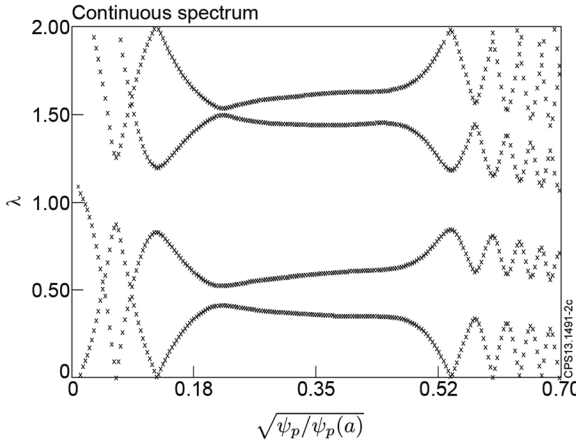


FIG. 10. Radial structure of the $n = 20$ Alfvén continuum in a 15MA ITER baseline case with $q(0) = 0.9$. Here, $\lambda = \omega R_0/V_A(0)$ and $\sqrt{\psi_p/\psi_p(\text{edge})} \approx r/a$.

continuum for this case computed with the CSCAS code.¹⁶ In the core region, $r/a \cong 0.2$, the magnetic shear is quite low, $S \cong 0.016$, so LSTAEs that require a very low-shear ordering, $\varepsilon/S \geq 1$, may exist. Indeed, such modes are found with the spectral MHD MISHKA code,¹⁷ and Figure 11 shows anti-symmetric LSTAE computed with an eigenfrequency near the top of the TAE gap. Since the radiative damping of such LSTAE is weaker than that of their symmetric LSTAE counterparts,¹⁸ and their damping is relatively insensitive to the plasma pressure,¹³ such modes are of interest in the core region. Note, however, that due to the narrow radial width of the LSTAE, an example of which is shown in Figure 11, and the relatively narrow band of toroidal mode numbers for which TAE gaps exist in this region (see Figure 7), the TAE-induced radial transport of alpha-particles will be limited to the region of mode localisation in the case that such LSTAEs were indeed excited. In such case, the main effect may be a redistribution of alpha-particles and beam ions from inside to outside the $q = 1$ surface. The principal consequence in such a case could be a change to the sawtooth stability, which can be stabilised by energetic ions, as has been observed on JET.¹⁹

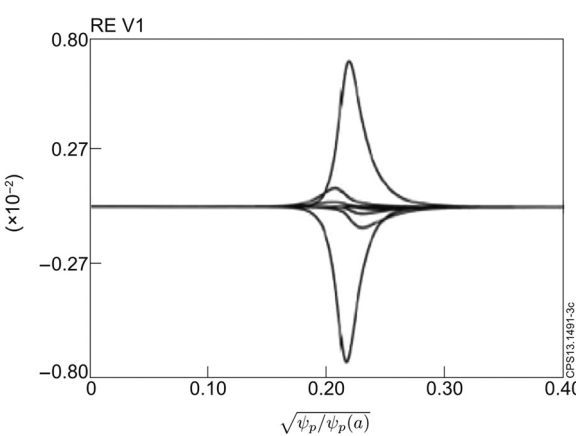


FIG. 11. Upper core-localised TAE with $n = 20$ and $\lambda = 0.525$ in the 15MA ITER baseline case with $q(0) = 0.9$. Here, $V_1 = s \cdot V_r$, V_r is the radial velocity component and $\sqrt{\psi_p/\psi_p(\text{edge})} \approx r/a$.

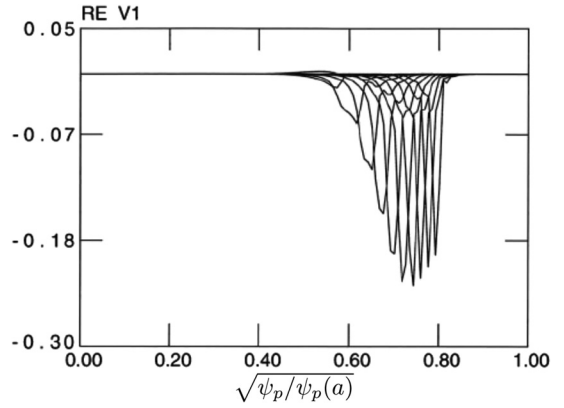


FIG. 12. Global TAE with $n = 20$ and $\lambda = 0.447$ in the 15MA ITER baseline case with $q(0) = 0.9$.

In the external region, $r/a > 0.5$, the magnetic shear becomes high, $S \cong 1$ at $r/a \cong 0.6$ and $S \cong 1.5$ at $r/a \cong 0.7$. Here, the distance between TAE gaps becomes smaller than the width of the TAE poloidal harmonics, $r_{TAE}/(nS) < r_{TAE}/m$, so that global TAEs can exist that span the plasma's minor radius. Figure 12 shows a result from the MISHKA code for a TAE with $n = 20$ consisting of ~ 10 poloidal harmonics. These modes are quite extended in radius and for every n there are many of them, with somewhat different eigenfrequencies. It should be recalled that since Figures 11 and 12 are the result of eigenmode analyses, the amplitudes of the eigenvectors (V_1 in this case) are undetermined and cannot be compared.

The EAE gaps can be investigated in a similar manner to those of the TAE with an example shown in Figure 13.

For the EAE gaps, similar to those of the TAE, two distinct radial regions are found in the plasma core and the external region. Low-shear EAE (LSEAE) modes are found to exist in the core region analogous to the LSTAE found above. Figure 14 shows an example of an $n = 20$ LSEAE computed with the MISHKA code for the 15MA ITER baseline equilibrium with $q(0) = 0.9$. In contrast to the LSTAEs, which can exist at the bottom and the top of the TAE frequency gap with the number of TAE-frequencies per gap being

$$p_{TAE} \approx \varepsilon/S. \quad (7)$$

LSEAEs have their eigenfrequencies near the top of the EAE gap only, whilst the number of eigenvalues per EAE-gap is²⁰

$$p_{EAE} \approx \sqrt{e/S}, \quad (8)$$

where

$$e \equiv \frac{\kappa^2 - 1}{\kappa^2 + 1} = \frac{(b/a)^2 - 1}{(b/a)^2 + 1}$$

is the ellipticity parameter in a straight field line coordinate system. Furthermore, similar to TAE, global EAEs can be formed in the external region. Figure 15 shows such an $n = 20$ EAE.

To conclude this section, it is necessary to note that the nearly constant density and weak magnetic shear in the core

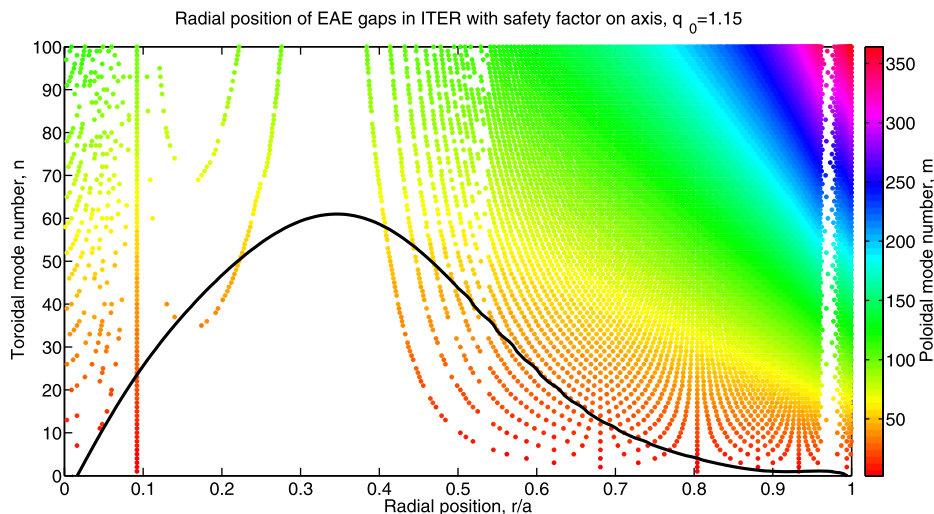


FIG. 13. Radial localisation of EAE gaps in the 15 MA ITER baseline case with $q(0) = 1.15$.

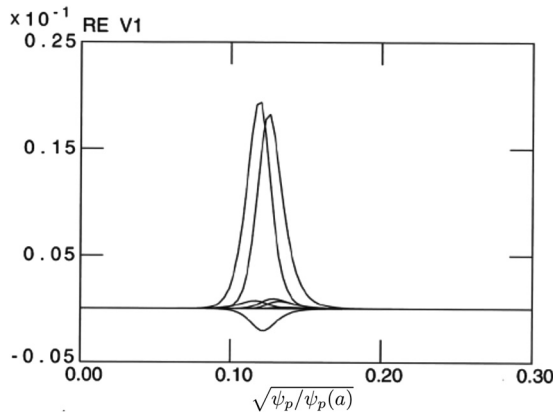


FIG. 14. Core-localised EAE with $n = 20$ and $\lambda = 1.15$ in 15MA ITER baseline case with $q(0) = 0.9$.

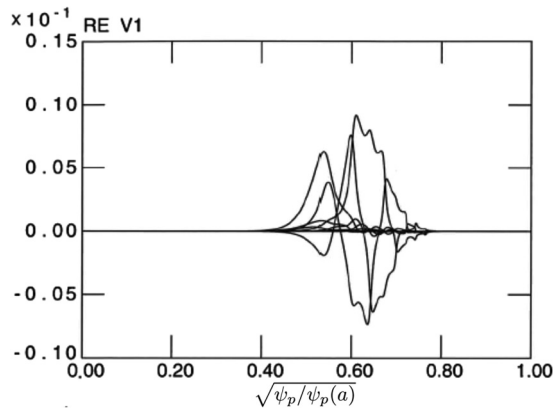


FIG. 15. Global EAE with $n = 20$ and $\lambda = 1.036$ in 15MA ITER baseline case with $q(0) = 0.9$.

region significantly reduce the (usually high) Alfvén continuum damping of a “local” Alfvén wave packet satisfying the shear Alfvén wave (SAW) dispersion equation. The residual damping of such Alfvénic “quasi-modes” can be assessed in a similar manner to that described in Ref. 21. The effect of alpha-particle and beam ion gradients could provide the

conditions for the existence of Energetic Particle Modes (EPMs).²² Such modes should also be investigated, in addition to weakly damped TAE and EAE.

IV. LANDAU DAMPING OF TAE DUE TO THERMAL IONS

The damping of Alfvén eigenmodes by thermal D and T ions is the main effect competing with the alpha-particle drive in the mode excitation. In this section, local estimates of the thermal ion damping effects are presented, which are expected to play a major role in determining overall TAE stability. The sensitivity of thermal ion Landau damping to the ion temperature and ion composition, both of which vary during an ITER discharge, is also investigated. The thermal ion species in the burning ITER plasmas under consideration will be represented by four main types⁸

$$\begin{aligned} \text{D : } & m_{\text{D}} = 2m_{\text{H}}, \quad e_{\text{D}} = e_{\text{H}}; \\ \text{T : } & m_{\text{T}} = 3m_{\text{H}}, \quad e_{\text{T}} = e_{\text{H}}; \\ \text{He : } & m_{\text{He}} = 4m_{\text{H}}, \quad e_{\text{He}} = 2e_{\text{H}}; \\ \text{Be : } & m_{\text{Be}} = 9m_{\text{H}}, \quad e_{\text{Be}} = 4e_{\text{H}}; \end{aligned}$$

where m_{H} and e_{H} are the mass and charge of a hydrogen ion. For these ions, the quasi-neutrality condition reads

$$n_e = n_{\text{D}} + n_{\text{T}} + 2n_{\text{He}} + 4n_{\text{Be}}, \quad (9)$$

and the main plasma ion depletion effect may be introduced as follows:

$$(n_{\text{D}} + n_{\text{T}})/n_e = 1 - \mu. \quad (10)$$

Here, the depletion factor is considered in the range

$$0.08 \leq \mu \ll 1, \quad (11)$$

where the lower boundary is determined by Be impurity ions, which are assumed to be always present in the plasma at the level of 2% (as given in Eq. (1)). Another major contributor to the depletion is the He ash population, the density of which is determined by the intensity of DT fusion and the efficiency of the He ash sink (transport and pump-out). The

D:T mixture in burning plasmas is targeted to be close to 50:50, so that

$$n_T/n_D = 1 - \delta, \quad |\delta| \ll 1. \quad (12)$$

It follows from Eqs. (9)–(12) that the ion densities are related to the electron density via

$$\frac{n_D}{n_e} = \frac{1 - \mu}{2 - \delta}; \quad \frac{n_T}{n_e} = \frac{(1 - \delta) \cdot (1 - \mu)}{2 - \delta}; \quad \frac{n_{He}}{n_e} = \frac{\mu}{2} - 0.04; \quad (13)$$

and that the Be density is given by Eq. (1). The value of the Alfvén velocity is

$$V_A = \frac{B_0}{\sqrt{\mu_0 m_H (2n_D + 3n_T + 4n_{He} + 9n_{Be})}} \\ = \frac{B_0}{\sqrt{\mu_0 m_H n_e \cdot 2.43 \cdot (1 - 0.2\mu - 0.08\delta)}}, \quad (14)$$

showing a somewhat higher sensitivity to the plasma depletion than to a deviation in the D:T mixture from the optimum value 50:50. For optimal ITER parameters, i.e., $\mu = 0.08$ and $\delta = 0$, we have

$$V_A = 7 \times 10^6 \text{ m/s} < V_{beam}(t = 0) = 10^7 \text{ m/s} < V_x(t = 0) \\ = 1.3 \times 10^7 \text{ m/s}.$$

The damping of TAE due to thermal ions with Maxwellian distribution functions is determined by the Landau resonances of D ions at $V_{\parallel D} = V_A/3$ and by the T ions at $V_{\parallel T} = V_A/3$, while the contribution from Maxwellian He ash is small due to the low density and heavy mass of the He ions. The total thermal ion damping is the sum of the linear contributions from D ions and T ions,

$$\gamma_i = \gamma_D + \gamma_T, \quad (15)$$

where^{23,24}

$$\frac{\gamma_D}{\omega} \approx -\frac{\sqrt{\pi}}{4} q^2 \beta_D x_D \left(1 + (1 + 2\tau_D + 2x_D^2)^2 \right) \exp(-x_D^2), \quad (16)$$

and γ_T is given by a similar expression with index T instead of D. Here, the term with $\tau_D = T_e/T_D$ is due to the finite parallel electric field of TAE, and

$$x_D = \frac{V_A}{3V_D}. \quad (17)$$

In the ITER baseline case considered here, the thermal plasma beta is $\beta_{therm}(0) = 6.84\%$, so the beta values of the thermal species are estimated (neglecting the impurities) as

$$\beta_e(0) = 3.68\%, \quad \beta_D(0) = \beta_T(0) = 1.58\%,$$

for $n_T/n_D = 1$, and the proportion between D and T varies in accordance with Eq. (12).

It is possible to combine the damping effects due to D and T ions to obtain

$$\frac{\gamma_i}{\omega} = \frac{\gamma_D}{\omega} \cdot \left[1 + \frac{n_T}{n_D} \sqrt{\frac{3}{2}} \left(\frac{1 + x_D^2}{1 + (2/3)x_D^2} \right)^2 \exp\left(-\frac{x_D^2}{2}\right) \right], \quad (18)$$

so the relative contribution of T ions can be easily assessed. It is interesting to note that the relative weight of the T ion contribution given by the second term in Eq. (18) depends exponentially on the ion temperature. In particular, as the ion temperature decreases, the ion Landau damping due to T ions becomes negligible before the ion Landau damping due to D ions. Physically, this is due to the higher mass of T ions, which means that their thermal velocity is lower than that of D ions (at similar temperatures, $T_T = T_D$), so the damping due to T ions is smaller than that of D ions with same density. For typical ITER parameters, $B_0 = 5.3$ T, $n_e = 10^{20} \text{ m}^{-3}$, and $T_T = T_D = 20 \text{ keV}$, one has

$$x_D = 1.74, \quad x_T = x_D \sqrt{3/2} = 2.1, \quad (19)$$

so the contribution of T ions is about half that of the D ion contribution,

$$\frac{\gamma_i}{\omega} = \frac{\gamma_D}{\omega} \cdot \left[1 + 0.484 \frac{n_T}{n_D} \right]. \quad (20)$$

Figure 16 displays the relative importance of T ion damping versus the D ion damping as a function of the ion temperature for a range of D:T concentrations and plasma depletion factors.

For δ and μ small, the ion Landau damping in the vicinity of thermal D velocity corresponding to $x_{D0} = 1.74$ can be expressed as

$$\frac{\gamma_i}{\omega} \approx -\frac{\sqrt{\pi}}{8} \beta_e q^2 x_{D0} \left(1 + 2\tau_D + 2x_{D0}^2 \right)^2 e^{-x_{D0}^2} \\ \times (1 - 1.3\mu + 0.26\delta)[1 + 0.5(1 - 1.1\delta - 0.24\mu)]. \quad (21)$$

It is again seen that the effect of the main ion depletion, μ , acts on the ion damping more strongly than the effect of the deviation from the optimum D:T mixture, δ .

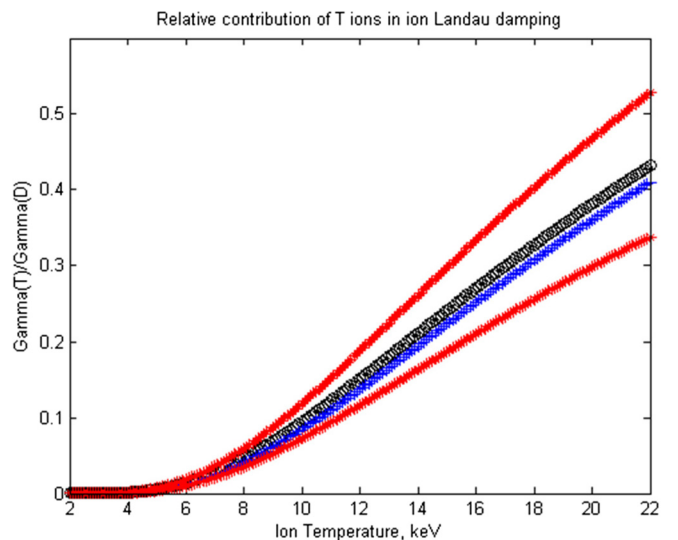


FIG. 16. Ratio of T ion Landau damping to D ion Landau damping as a function of ion temperature. The black line corresponds to $\mu = \delta = 0$, the blue line corresponds to $\mu = 0.2, \delta = 0$, and the upper and lower red lines correspond to $\mu = 0$ and $\delta = -0.2$ and $\delta = +0.2$, respectively.

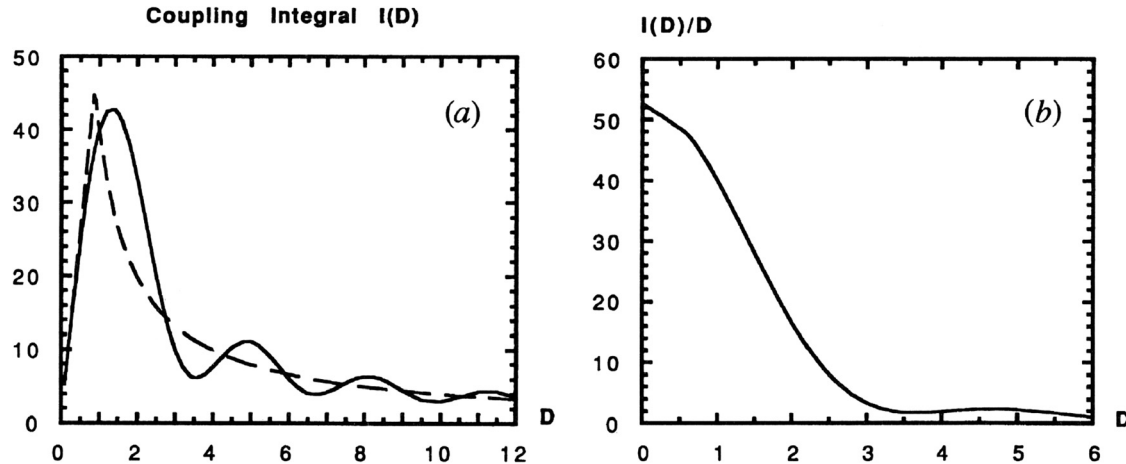


FIG. 17. Coupling integral $I(D)$ for passing alpha-particle principal resonances: (a) asymptotic expression (broken curve) and numerical result (full curve); (b) function $I(D)/D$ used in Eq. (22). Reprinted with permission from B. N. Breizman and S. E. Sharapov, "Energetic particle drive for toroidicity-induced Alfvén eigenmodes and kinetic toroidicity-induced Alfvén eigenmodes in a low-shear tokamak," *Plasma Phys. Controlled Fusion* **37**(10), 1057 (1995). Copyright 1995 IOP Publishing. Reproduced by permission of IOP Publishing. All rights reserved.

Equation (16) shows that the total (D and T) thermal ion Landau damping is exponentially sensitive to the temperature of thermal ions, so in the region of interest shown in Figure 2, $2\text{keV} \leq T_D = T_T \leq 22\text{keV}$, the role of ion Landau damping may go from "very stabilising," $\gamma_{D+T}/\omega > 1\%$, to insignificant, $\gamma_{D+T}/\omega < 0.1\%$. Figure 18 illustrates this temperature dependence.

V. TAE DRIVE DUE TO ALPHA-PARTICLES AND NBI-PRODUCED D IONS

The alpha-particle drive may be assessed using the local estimate calculated in¹²

$$\frac{\gamma_\alpha}{\omega} = -\frac{3}{32\pi}\varepsilon q \frac{d\beta_\alpha}{dr} \frac{V_A^2}{V_0^2} \int_{V_A}^{V_0} dV \frac{V_A^2 + V^2}{V^2} \cdot \frac{I(D)}{D}, \quad (22)$$

where V_0 is the alpha particle birth speed ($1.3 \times 10^7 \text{ m/s}$) and the finite drift orbit parameter D for passing alpha-particles resonating with a TAE via the $V_{||\alpha} = V_A$ resonance is given by

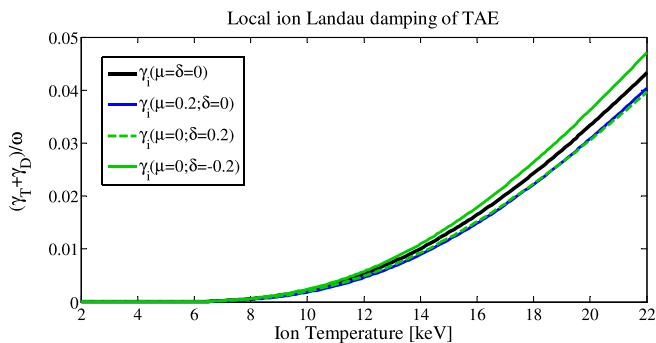


FIG. 18. Local Landau damping of TAE, $|\gamma_D + \gamma_T|/\omega$, as a function of ion temperature. Maxwellian distributions of thermal D and T ions are assumed, and the resonances $V_{||i} = V_A/3$ between TAE and the ions are considered. The black line corresponds to $\mu = \delta = 0$, the blue line corresponds to $\mu = 0.2$, $\delta = 0$, and the upper and lower green lines correspond to $\mu = 0$ and $\delta = -0.2$ and $\delta = +0.2$, respectively.

$$D = \frac{qm(V_A^2 + V^2)}{2V_A r_{AE} \omega_{B\alpha}}, \quad (23)$$

and the coupling integral $I(D)$ computed in the low-shear approximation for TAE is shown in Figure 17.

For the ITER 15 MA baseline scenario under consideration with the profiles shown in Figures 1–3, the thermal ion Landau damping is shown in Figure 18. In Figures 19 and 20, the thermal ion Landau damping is compared with the expected alpha-particle excitation.

Figures 19 and 20 indicate that estimates for the alpha-particle drive for TAE could exceed the thermal ion Landau damping in the outer region only, $r/a > 0.5$, with the maximum net drive $(\gamma_\alpha - |\gamma_D + \gamma_T|)/\omega \cong (1.5 \div 2) \times 10^{-3}$. However, due to the global radial structure of the TAE modes expected in the outer region, a global numerical stability analysis should be employed that takes into account all the contributions across the whole radially extended TAE-mode structure.

Taking into account that the 1 MeV deuterium beam will be injected tangentially, the contribution of the beam ions to the TAE stability should also be assessed. The local

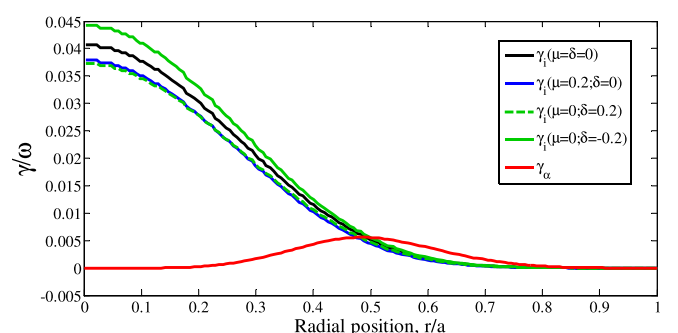


FIG. 19. Local Landau damping of TAE due to D and T ions and alpha-particle drive versus normalized radius. The alpha-particle drive is shown in red, while the black line corresponds to the ion Landau damping at $\mu = \delta = 0$, the blue line corresponds to $\mu = 0.2$, $\delta = 0$, and the two green lines correspond to $\mu = 0$, $\delta = \pm 0.2$.

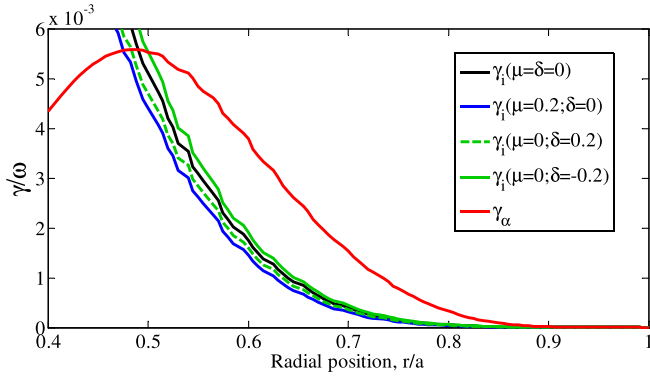


FIG. 20. Zoom of Figure 19. Local Landau damping of TAE due to D and T ions (black line: $\mu = \delta = 0$; blue line: $\mu = 0.2, \delta = 0$; and green lines: $\mu = 0, \delta = \pm 0.2$) and alpha-particle drive (red line) versus normalized radius for $0.4 \leq r/a \leq 1.0$.

drive due to the beam may be estimated in accordance with Ref. 12 as

$$\frac{\gamma_\alpha}{\omega} = -\frac{15}{16\pi} q^2 r_{AE} \frac{d\beta_{beam}}{dr} \cdot \frac{V_A^2}{V_0^2} \cdot \frac{I(D)}{D}, \quad (24)$$

where the finite drift orbit parameter D is given by

$$D = \frac{qmV_A}{r_{AE}\omega_{Bb}}, \quad (25)$$

and the coupling integral is as shown in Figure 17. Due to the strongly anisotropic distribution function of the beam, the beam drive is comparable to the alpha particle drive though the beam has a lower power. Figure 21 shows how the beam drive compares to the alpha-drive, while Figure 22 shows how the sum of the two drives compares to the thermal ion Landau damping. It is seen that the beam could expand the TAE instability region, from $r/a \geq 0.5$ to $r/a \geq 0.4$.

In Secs. VI and VII, some additional damping mechanisms affecting TAE are discussed.

VI. TRAPPED ELECTRON COLLISIONAL DAMPING OF TAE

Trapped electron collisional damping^{24,25} is associated with electron pitch-angle collisional scattering in the

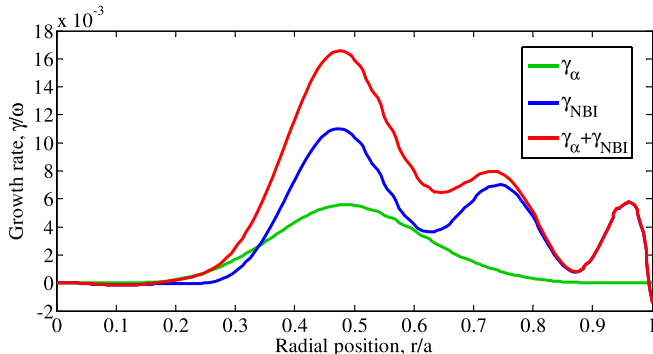


FIG. 21. Alpha-particle drive (green) and NBI-drive (blue) and sum of the two (red) versus normalized radius.

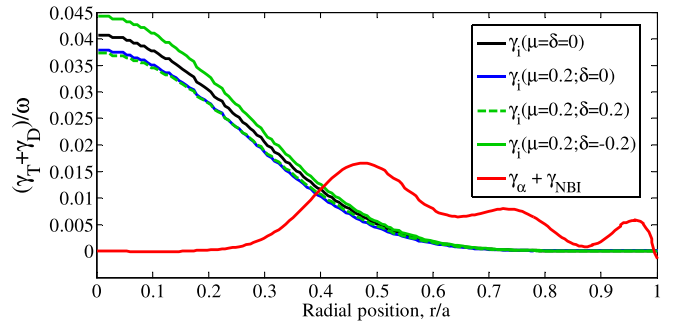


FIG. 22. The sum of alpha-particle and beam drives (red) versus ion Landau damping, as shown in Figure 19, versus normalized radius.

presence of a TAE perturbation. Although this damping is usually small, it is proportional to m^2 and so plays an important role in extracting energy from waves with short wavelength scales. The damping may be estimated as²⁴

$$\frac{\gamma_e}{\omega} = -\sqrt{\frac{\nu_e}{\omega}} \left(3.9\beta_e q^2 + 0.44 \left(\frac{\rho_S m}{r} \right)^2 \right) \left[\ln \left(16 \sqrt{\frac{\epsilon\omega}{\nu_e}} \right) \right]^{-3/2}. \quad (26)$$

Figure 23 shows the value of this local estimate for the ITER profiles presented in Figures 1–3, together with the ion Landau damping and the alpha-particle and beam drives. It is seen that the overall effect of trapped electron collisional damping for the considered $n = 30$ case of the most unstable TAEs is small and can be neglected except at the plasma edge where it can overcome the alpha-particle drive ($r/a \geq 0.8$) but not the beam drive.

VII. RADIATIVE AND CONTINUUM DAMPING EFFECTS ON TAE

Radiative TAE damping^{25–27} is caused by the small, but finite, coupling between TAE and Kinetic Alfvén Waves (KAWS), which carry away wave energy in the radial direction with increasing k_r , $k_r \rightarrow \infty$. The damping is sensitive with respect to the mode width and to whether the mode eigenfrequency is located at the top or the bottom of the corresponding TAE-gap.¹⁸ The sensitivity of the radiative damping to the mode width implies that plasma pressure, through a narrowing of the mode width, can increase the

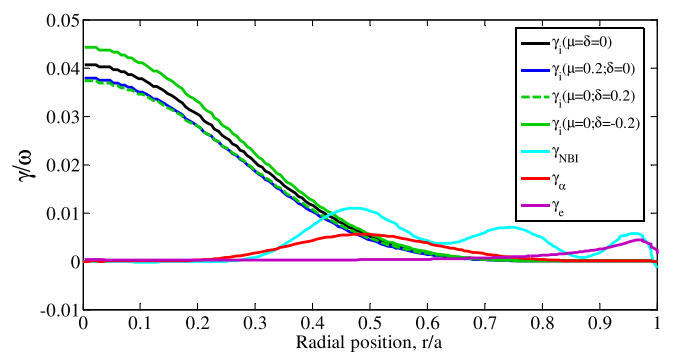


FIG. 23. Trapped electron collisional damping (purple). Local Landau damping of TAE due to D and T ions as shown in Figure 19, alpha-particle drive (red) and beam drive (cyan).

radiative damping significantly unless the mode frequency is close to the top of the TAE gap.¹⁸ In general, a kinetic analysis is required for assessing the role of the radiative damping, but analytical expressions may be used in the limiting cases of small and large magnetic shear. In particular, for TAE with frequencies at the bottom of the gap, the following expressions may be used:²⁴

$$\frac{\gamma_{rad}}{\omega} = -\frac{\pi^2}{8}\epsilon S^2 \exp\left(-\frac{\pi^3 S^2}{2^{7/2}\lambda}\right), \quad S \ll 1, \quad (27)$$

$$\frac{\gamma_{rad}}{\omega} = -\frac{\pi^{3/2}}{48}\epsilon \frac{\lambda^a}{S^4} \exp\left(-\frac{2^{5/2}}{3\lambda}\right), \quad a \cong \frac{\pi^2 \sqrt{2}}{144 S^4 \lambda}, \quad S \geq 1, \quad (28)$$

where $S = \frac{rq'(r)}{q(r)}$; $\epsilon \approx \frac{5}{2} \frac{r}{R}$;

$$\begin{aligned} \lambda^2 &\equiv 16 \left(\frac{m\rho_i}{r} \right) \frac{S^2}{\epsilon^3} \left(\frac{3}{4} + \frac{T_e}{T_i} (1 - i\delta(v_e)) \right); \\ \delta(v_e) &\simeq 0.44 \sqrt{\frac{v_e}{\omega}} \left(\ln 16 \sqrt{\frac{\epsilon\omega}{2v_e}} \right)^{-\frac{3}{2}}; \end{aligned} \quad (29)$$

and v_e is the electron collision frequency.

In the peripheral region of interest, $r/a \geq 0.5$, the analytical estimate of the radiative damping is small, as shown in Figure 24.

Finally, continuum damping of TAE can occur due to the resonant interaction of a TAE with the Alfvén continuum if the radial structure of the Alfvén continuum crosses the TAE eigenfrequency at some radius. This damping can vary from zero in the case of an open TAE frequency gap, to a high value when the TAE frequency gap is closed, i.e., it is impossible to find any TAE frequency not intersecting the continuum at some radius. This effect was experimentally validated on JET, where the TAE damping measured with the external TAE antenna varied from 0.6% in the open TAE gap case, to a very high value of 5%, in the case of a closed TAE gap. In the limiting case of very high mode numbers and when the TAE gap is closed, an expression for the continuum damping was obtained in Refs. 28 and 29 to be

$$\frac{\gamma_{cont}}{\omega} \cong -0.8 \frac{S^2}{m^{3/2} \sqrt{\epsilon}}. \quad (30)$$

If the TAE frequency gap in the ITER baseline case under consideration were to be closed (contrary to that found and

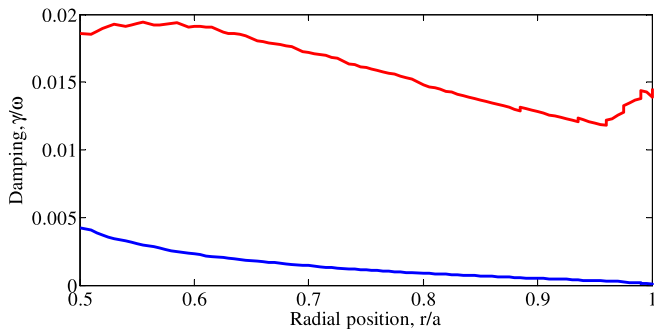


FIG. 24. Analytic expressions for the radiative (blue) and continuum (red) damping effects corresponding to the high-shear region. A closed TAE frequency gap is assumed when calculating the continuum damping.

shown in Figure 10), Eq. (30) would indeed provide a reasonably high damping rate in the external region of interest. Figure 24 shows that in this case, the damping could be in the range of 1.2%–1.9%, i.e., in excess of the net drive shown in Figure 23.

VIII. SUMMARY OF ALFVÉN EIGENMODE STABILITY FROM ANALYTIC ESTIMATES

In summary, analytic estimates have identified two very different radial regions in the plasma corresponding to the $Q = 10$ ITER baseline operational point with 15 MA

- (1) A core plasma region, $r/a \leq 0.5$, in which the majority of the alpha-particle population is confined, $q(r)$ is rather flat, and TAE and EAE gaps are scarce. In this region, thermal ion Landau damping completely dominates over the sum of the energetic particle drives arising from the alpha-particle and beam ion populations;
- (2) An external plasma region, $r/a \geq 0.5$, where the alpha population is reduced, but the TAE frequency gap density is high (meaning all TAEs are global). In this region, the total drive due to alpha-particles and NBI-produced ions exceeds the ion Landau damping giving a net drive of $\gamma/\omega \sim 10^{-2}$.

Taking into account the multiplicity of TAE and EAE gaps in the external region, a global analysis of the linear TAE instability is required for $r/a \geq 0.5$ to improve the accuracy of the local estimates. Evaluating the nonlinear evolution of TAE in this region will require further studies with multiple modes at multiple frequencies. However, the population of alpha-particles in the external region is relatively low and so any TAE-induced redistribution is not expected to influence the burn process; only energetic ion losses to the first wall may be an issue.

IX. GOING BEYOND ANALYTIC ESTIMATES

In this section, the linear gyrokinetic code LIGKA^{30–32} is employed to carry out local and global calculations concerning the linear properties of TAEs in the scenario discussed in Sec. II. Due to the sensitivity of global mode stability on the radial profiles of the background quantities and the energetic particle distribution functions, a complete analysis for this scenario is not possible; however, a first set of representative parameters are investigated, also in view of benchmarking the code.

The equations solved by LIGKA are the quasi-neutrality (QN) equation and the gyrokinetic moment equation (GKM) that together with the gyrokinetic equation for the particle distribution function form a consistent model for electromagnetic perturbations in tokamak geometry. This implies that ion and electron Landau damping, radiative damping, and continuum damping are consistently included in this analysis. Starting directly from the equations as implemented in LIGKA, a rather general dispersion relation can be derived^{33–36} that allows analysis of the continuum solutions and the local damping due to electron and ion Landau damping:

TABLE I. Alfvén frequencies for different plasma compositions.

Plasma composition	Alfvén frequency
100% deuterium	196 kHz
100% tritium	160 kHz
50:50 D-T	175 kHz
50:50 D-T, He ash, Be	178 kHz
66:33 D-T, He ash, Be	183 kHz
22:66 D-T, He ash, Be	176 kHz

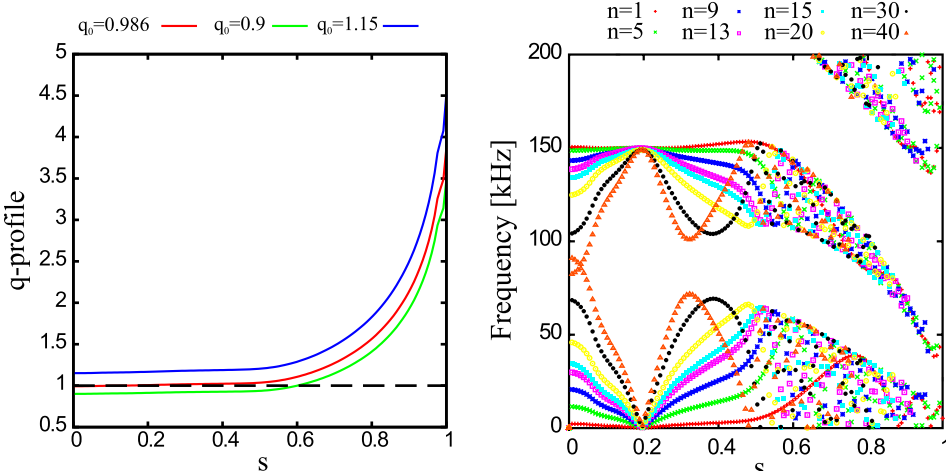
$$\begin{aligned} \frac{\omega^2}{\omega_A^2} \left(1 - \frac{\omega_p^*}{\omega} \right) - \bar{k}_{\parallel m}^2 R_0^2 \\ = \sum_{a=i,e} 2 \frac{v_{th,a}^2}{\omega_A^2 R_0^2} \left(- [H(x_{a,m-1}) + H(x_{a,m+1})] \right. \\ \left. + \tau_a \left[\frac{N^m(x_{a,m-1}) N^{m-1}(x_{a,m-1})}{D(x_{a,m-1})} \right. \right. \\ \left. \left. + \frac{N^m(x_{a,m+1}) N^{m+1}(x_{a,m+1})}{D(x_{a,m+1})} \right] \right), \quad (31) \end{aligned}$$

where a is the summation index over electrons and all background ion species and $\bar{k}_{\parallel m}^2$ stands for the parallel wave vector including the toroidal coupling up to leading order in ϵ , e.g., $\bar{k}_{\parallel m}^2 = (k_{\parallel m}^2 + k_{\parallel m+1}^2 \pm \sqrt{(k_{\parallel m}^2 - k_{\parallel m+1}^2)^2 + 4\epsilon^2 r^2 k_{\parallel m}^2 k_{\parallel m+1}^2}) / (2(1-\epsilon^2 r^2))$, where $\epsilon = 5r/2R_0$.^{10,37,38} Further,

$$\begin{aligned} x_{a,m} &= \frac{\omega}{|k_{\parallel m}| v_{th,a}}; \quad v_{th,a} = \sqrt{\frac{2T_a}{m_a}}; \\ \omega_p^* &= \sum_i \frac{k_\theta}{eBn_i} \frac{\partial p_i}{\partial r} \frac{m_i n_i}{m_{eff} n_e}; \quad \text{and} \quad \tau = T_e/T_a. \end{aligned}$$

The definitions for the polynomials H , N , and D including the complex plasma dispersion function can be found, for example, in Refs. 33 and 36. The upper index m in $N^m(x_{m-1})$ refers to the poloidal mode number, m , to be used in $\omega_m^* = \frac{T_i}{eB} k_{m,\theta} \frac{\nabla n}{n}$.

This very general dispersion relation given in Eq. (31) describes the linear physics of shear Alfvén waves in tokamak geometry (left hand side) and their modification due to



the coupling to acoustic and kinetic ballooning waves up to first order in ϵ (right hand side).

Since this dispersion relation can be derived directly from the equations that are the basis for LIGKA, all simplifications concerning the geometry and v_\perp ($v_\perp = 0$) that are assumed when expanding the drift operator can be dropped if the coefficients and the matrix elements of the GKM and the QN equations are calculated numerically.³⁶ Although the influence of the elongation of flux surfaces³⁹ and deeply trapped particles⁴⁰ on the dispersion relation has been analytically examined, in general, it is necessary to numerically evaluate the coefficients in Eq. (31). The LIGKA code has been benchmarked^{36,41} to recover the analytical dispersion relation in the appropriate limit.

As indicated by the definition of ω_p^* and the sum on the right hand side of Eq. (31), in this version of the dispersion relation the thermal ion species are treated separately, i.e., their orbit and profile properties are taken into account explicitly in order to account for the D-T mixture and dilution effects due to helium ash and beryllium impurities.

For reference, in Table I the on-axis values for $f_A = v_A/(2\pi R_0)$ for different plasma compositions are given. Note that the concentration of He is kept constant in the cases where the D-T mix is varied. Furthermore, in order to fulfil quasi-neutrality, in the D-T case $n_D = n_T = n_e/2$ was assumed, whereas in the other cases the profiles given in Sec. II are assumed. Very small corrections to the Be density were necessary to exactly fulfil the quasi-neutrality requirement.

A. Ideal MHD spectra and TAE location

In order to compare to the analytic results of Secs. III–VII, the ideal MHD SAW spectra are plotted for three different q -profiles: $q_0 = 0.986$, 0.9, and 1.15 (see Figure 25). The first case is identical to the calculation with the MISHKA code in Sec. III, whereas the other two cases are obtained by scaling the same equilibrium with a different q_0 , i.e., the total current is not kept constant but rather varied by $\sim 10\%$. Instead, the shear is kept constant, meaning that also the $q = 1$ surface is shifted outwards with respect to the case ($q_0 = 0.9$) in Sec. III. Therefore, the cases for $q_0 = 0.9$ can be seen as a sensitivity analysis with respect to the

FIG. 25. Left: The different q -profiles used in the simulations versus the normalized poloidal radius s ; right: Ideal SAW continuum for $q_0 = 0.986$ versus the normalized poloidal radius s .

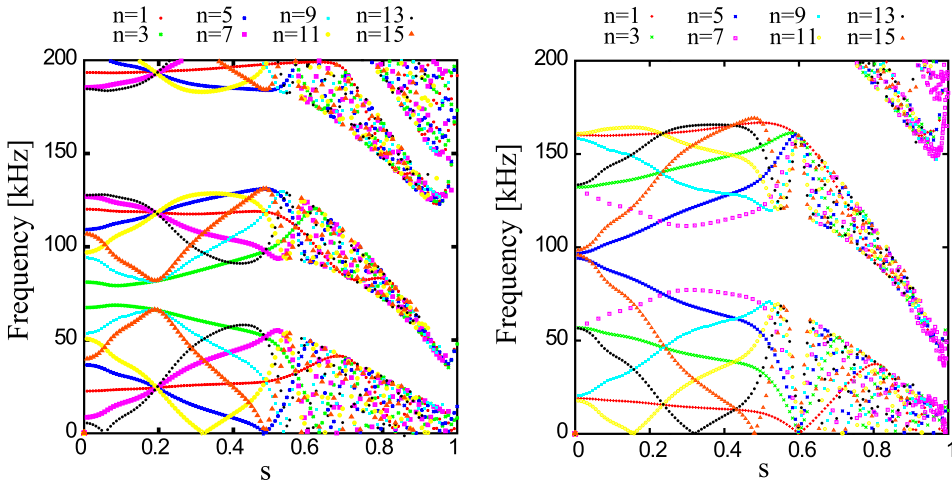


FIG. 26. Left: Ideal SAW continuum for $q_0 = 1.15$ versus the normalized poloidal radius s ; right: Ideal SAW continuum for $q_0 = 0.9$ versus the normalized poloidal radius s .

q -profile: whereas $s = 0.1$ is probably a lower limit for the position of the $q = 1$ surface, $s = 0.58$ is an upper limit. Similar considerations are true for the case with $q = 1.15$.

The incompressible shear Alfvén continuum for the three cases is shown in Figures 25 and 26. For $q_0 = 0.986$, the TAE gap for low- n TAEs is outside $s \geq 0.45$ due to the proximity of q to 1. The gaps are closed, for the symmetric TAEs at the bottom of the gap at around $s \sim 0.8$ and for the anti-symmetric TAEs at $s \sim 0.6$. For the case where the total current is kept constant, this intersection position might vary slightly due to a steeper/flatter q -profile, however, the closed gap would not open due to such a modification.

B. Local kinetic analysis

The dispersion relation given in Eq. (31) with numerically determined coefficients is used to identify the local ion and electron Landau damping—similar to the procedure in the earlier analytic sections. In the following, the damping is quoted as a percentage of the real mode frequency. An example is shown for $n = 8$, $q_0 = 0.9$ in Figure 27.

Compared to the ideal, reduced MHD results, considerable corrections due to the coupling to the sound waves can be seen to occur. However, these corrections cannot be captured properly by a constant compressibility since they are frequency dependent. As discussed in Sec. VII, the local damping is much smaller for the anti-symmetric mode in this

case since it has a higher frequency and the continuum accumulation point is further out ($s = 0.55$) and thus at lower temperature than the accumulation point for the symmetric TAE. Here, it is assumed that the TAEs are close to their respective accumulation points, as will be shown later. The calculated local damping that includes also the electrons, side-bands, and background gradient effects is relatively close to the values quoted by the analytical formula given in Eq. (18). Looking at higher mode numbers (see Figure 28), one can see that there can be considerable differences between neighbouring n 's due to their different spatial locations and frequencies, which depend upon the q -profile.

The damping can also be very small for low- n modes, as seen for the $n = 8$ mode in Figure 28, the anti-symmetric TAE branch (higher frequency) shows a very small damping rate at the frequency minimum, i.e., at the continuum accumulation point. Assuming that a global mode exists close to this point, this $n = 8$ anti-symmetric TAE is a good candidate for one of the least damped modes of the system with $\gamma/\omega \sim 0.3\%$. Located at mid-radius, $s \sim 0.5$, this mode is still in the region where it can experience a relatively strong energetic particle drive.

The next question to answer is the dependence on the background ion mixture. For the calculations shown above, four different ion species have been included as before: deuterium, tritium, thermal helium, and beryllium. For simulation efficiency, it is also of interest to address the question of

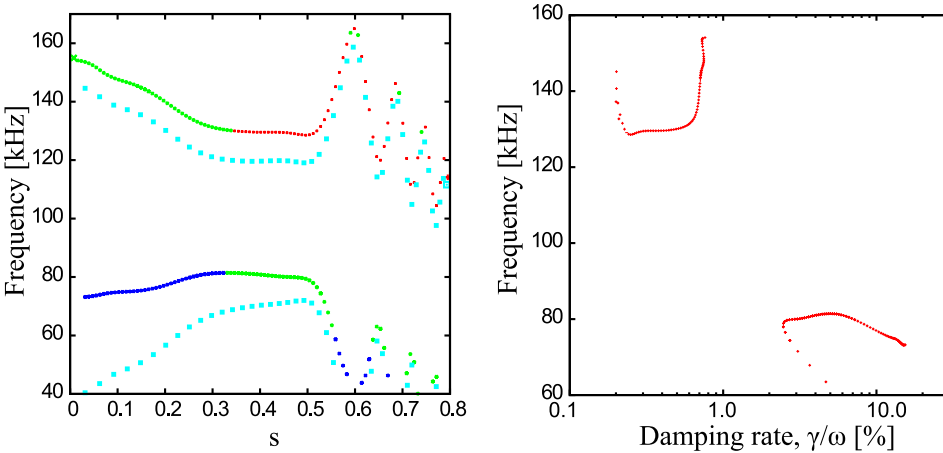


FIG. 27. Left: Kinetic continuum for $n = 8$ and $q_0 = 0.9$ versus the normalized poloidal radius s . In light blue, the reduced MHD calculation, in red the part of the continuum that has a damping less than $\gamma/\omega < 0.5\%$, in green $0.5\% < \gamma/\omega < 5\%$ and in dark blue $\gamma/\omega > 5\%$; right: The upper and lower TAE continuum branches as on the left as a function of the local damping. For a local estimate, the damping at the accumulation points (~ 125 kHz for the anti-symmetric branch and ~ 85 kHz for the symmetric branch) can be used. The damping is quite different: 0.3% vs. 5%.

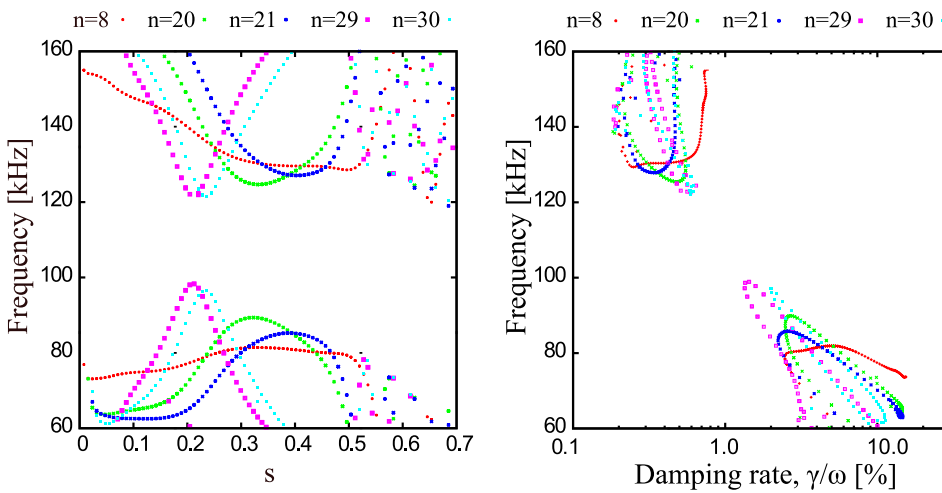


FIG. 28. Left: Kinetic continuum for $n = 8, 20, 21, 29, 30$ and $q_0 = 0.90$. Right: The upper and lower TAE continuum branches as on the left as a function of the local damping.

whether the D-T background can be represented by hybrid particles with a mass of $2.5m_H$. The results for this local damping calculation ($n = 8$) are shown in Figure 29. For the anti-symmetric TAE branch, where the damping is anyway low, there is hardly any influence on the damping due to background isotope effects. In fact, the simplest calculation with just one hybrid species results in a very minor error (<0.05%) compared to the full calculation with four species. (In all cases, with less than four species the densities were slightly adapted in order to exactly fulfil quasi-neutrality. Note, also that differences in the Alfvén velocities due to changes in the mass density were taken into account.) For the symmetric branch, the damping at the accumulation point is overestimated by 2.5% if the diluting effects of the background are neglected: the Maxwellian tail of the heavier ions resonates (i.e., Landau damps) much more weakly with the TAE frequencies due to their heavier mass compared to D. This effect will be even more pronounced when investigating the stability and excitation of low-frequency branches such as those associated with Beta-induced Alfvén Eigenmodes (BAEs), Alfvénic Ion-Temperature-Gradient modes (AITGs), and Kinetic Ballooning Modes (KBMs).

The variation of the D-T composition does not cause large differences in the damping. Figure 30 (left) shows the weak dependence of the local damping on the isotope mixture. Although the real frequencies change due to the

different mass, the damping at the upper (symmetric branch) and lower (anti-symmetric branch) accumulation points does not vary significantly. This is in agreement with the findings of Sec. IV where the effect of the main ion depletion, μ , was shown to act on the ion damping more strongly than the effect of the deviation from the optimum D:T mixture, δ .

On the right of Figure 30, the effect of including trapped particles is shown: A small frequency downshift (~5%) is found and the continuum shifts into the less damped region by ~1%. This correction is relatively small for the TAE frequency range but it has been found to be important for low-frequency modes like BAEs.⁴¹

In an MHD analysis of TAEs, diamagnetic effects are usually neglected; however, since the relevant quantity ω_p^* scales with poloidal mode number, large mode numbers are expected to show some dependence on the diamagnetic frequency. Figure 31 shows this influence on the kinetic spectrum for $n = 8$ and $n = 30$. As can be clearly seen, for high mode numbers, the diamagnetic frequency has a considerable destabilising effect, whereas for low mode numbers the differences are very small as expected for TAEs.

As a summary for this section on local analysis, one can say that all the kinetic effects considered here tend to reduce the local damping. In particular, isotope effects are found to have a considerable impact. Thus, these numerical results

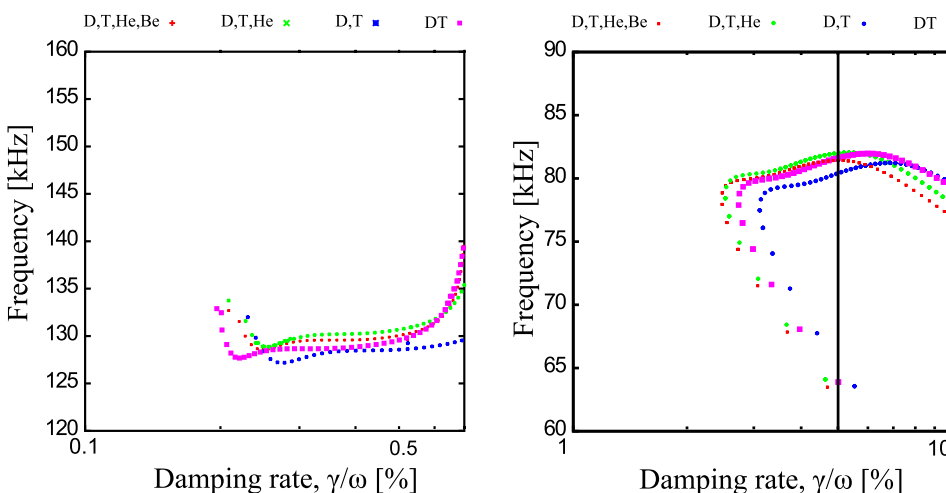
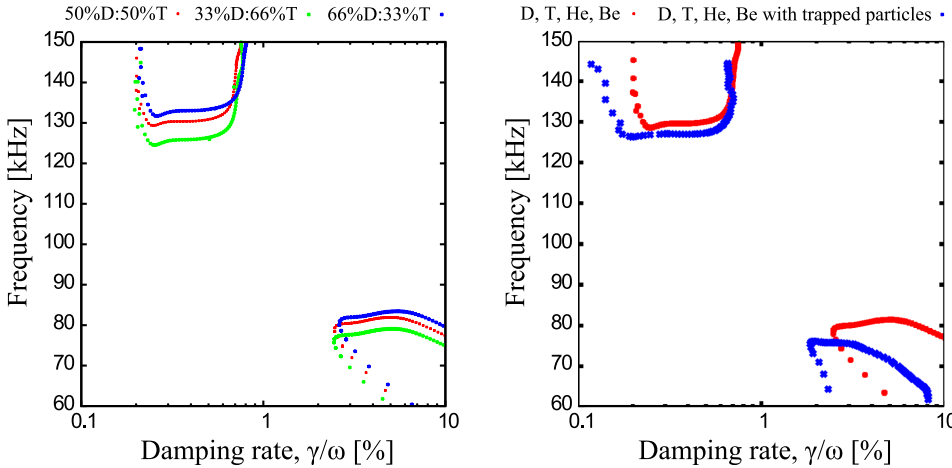


FIG. 29. Left: Kinetic continuum for the $n = 8$ anti-symmetric TAE branch for different isotope mixtures. There is a weak dependence of the damping at the accumulation point on different background ion components. The profiles of the He ash and the beryllium are as given in Sec. II. Right: Kinetic continuum for the $n = 8$ symmetric TAE branch. At low frequencies, considerable differences occur: the damping is overestimated by 2.5% if the diluting effects of the background are neglected (compare extrema of red and blue curves).



show very good agreement with the analytic work in Secs. III–VII, both qualitatively and quantitatively.

C. Global analysis

In Figures 32 and 33, some typical TAE mode structures for the equilibria described above are presented. Core-localised symmetric TAEs, edge-localised TAEs, and anti-symmetric TAEs can all be found. The symmetric TAEs, for e.g., $q_0 = 0.9$ (see Figure 33) are in the frequency range between $\omega_{TAE,even} = 0.44 - 0.50 \omega_A \approx 78 - 90$ kHz and the anti-symmetric TAEs between $\omega_{TAE,odd} = 0.67 - 0.70 \omega_A \approx 118 - 125$ kHz. The mode structures are very close to the MHD mode structures except for slightly different amplitudes of the poloidal harmonics due to small frequency shifts (arising from different sound wave coupling and diamagnetic corrections) and short wavelength features caused by finite Larmor radius effects.

Independently of whether they can be excited or not, of particular concern are low- n modes with a large radial extent and/or dense clusters of modes that cause overlapping resonances in phase space. In both cases, energetic particles can be effectively redistributed over a large radial region. For a definitive answer on the magnitude of such transport, global, non-linear calculations are necessary. Any local model will be correct for high- n modes only and although these modes are often the most unstable ones ($n \sim 30$), i.e.,

the modes with the largest drive and without continuum damping, it cannot be ruled out that low- n modes will be excited in regions of phase space that are not affected by the high- n modes—especially when they are sparse and only affect a small volume of phase space. The ideal spectra show that only in the case with $q_0 = 0.985$, i.e., q very close to 1, the TAEs between $n = 5$ and 35 fill the region between $0.35 < s < 0.6$ in a dense way. In the other cases, neighbouring n 's do not overlap continuously (see Figures 28 and 33). This “sparseness” of course depends crucially on the shape of the q -profile.

Moreover, in the non-linear phase the mode with the largest linear growth rate might not necessarily have the largest amplitude.^{42,43} Therefore, this linear analysis aims to analyse the question of how far global and intermediate- n modes are from the stability limits depending on various q -profiles. This information can be used for future hybrid non-linear multi-mode studies, for example, with the HAGIS model.⁴⁴

A full analysis of the different scenarios is beyond the scope of the analysis presented here. Therefore, a representative case is chosen in order to show the important trends. First, in the $q = 0.9$ scenario, some of the least damped modes of the system have rather low n , e.g., the $n = 8$ mode since it is localised at $s = 0.5$ and therefore avoids any strong ion Landau damping. These modes inside the $q = 1$ surface are often called “tornado” modes as the least unstable mode number changes with decreasing q_0 to lower n .

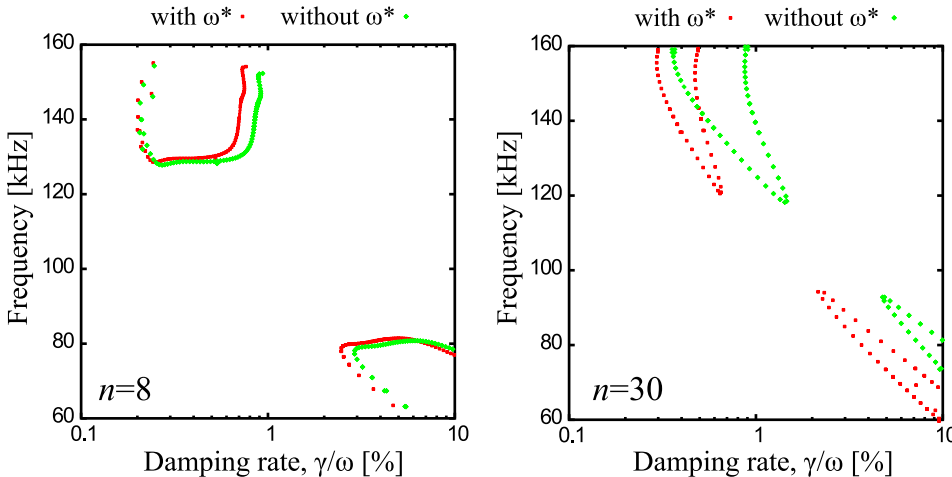


FIG. 31. Left: kinetic continuum for the $n = 8, m = 7, 8$ TAE branches with and without ω^* ; right: kinetic continuum for $n = 30, m = 29, 30$ with and without ω_p^* .

FIG. 30. Left: Kinetic continuum for the $n = 8$ symmetric and anti-symmetric TAE branch for different D:T mixtures. Although there is a small influence on the real frequency via a change of the mass density, the damping at the continuum accumulation point stays nearly constant. Right: Kinetic continuum for the $n = 8$ symmetric and anti-symmetric TAE branch including only circulating particles (red) and both circulating and trapped particles (blue). Whereas the higher frequency (odd) branch is not strongly affected, the lower frequency (even) branch shows reduced damping.

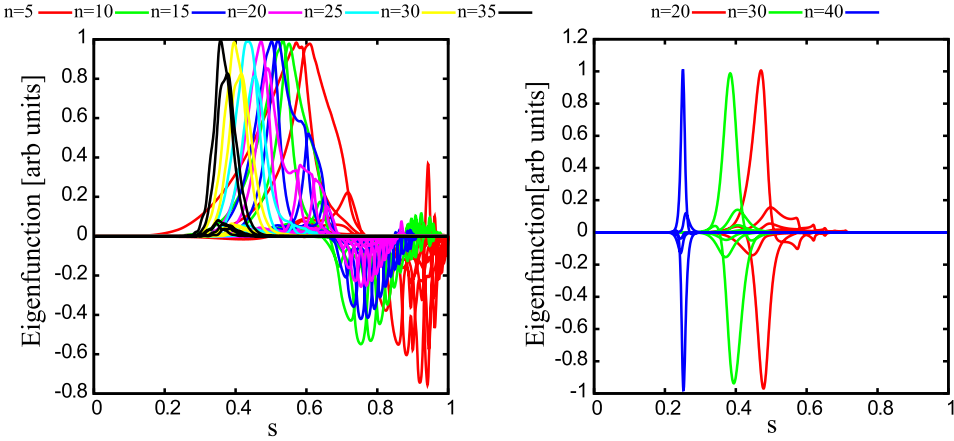


FIG. 32. Left: Eigenfunctions (electrostatic potential) for symmetric TAEs and $q_0 = 0.986$; right: Eigenfunctions (electrostatic potential) for anti-symmetric TAEs and $q_0 = 0.9859$.

values.^{19,45} The frequency and damping of the symmetric and anti-symmetric $n=8$ TAE in Figure 33 are 83.9 kHz, $\gamma/\omega = -0.82\%$ (symmetric) and 123 kHz, -0.67% (anti-symmetric). Adding the alpha particle drive using the β profile given in Figure 3 brings this anti-symmetric mode closer to marginal stability: $\gamma/\omega = -0.30\%$. Adding the on-axis NBI drive with the beam β -profile as given in Figure 4 (1 MeV birth energy, slowing down model) and an *ad hoc* model for the pitch angle distribution of the form $\exp\{-(\Lambda - \Lambda_0)^2/\Delta\Lambda^2\}$ with $\Lambda_0 = 0.2$, $\Delta\Lambda = 0.4$, and $\Lambda = \mu B_0/E$ drives the mode marginally unstable: $\gamma/\omega = +0.05\%$. More detailed calculations based on actual scenario modelling output for the velocity space distribution function (expected to have a non-negligible influence) will be the subject of future studies.

Since the neighbouring toroidal modes exhibit a much larger damping (more core localised) or a smaller drive (more edge localised), there will be no dense cluster of unstable modes and therefore any energetic particle transport is expected to be rather small.

In the case where $q_0 = 0.985$, the TAE instead form a rather dense cluster of modes where the mode peak location moves outwards with decreasing mode number (see Figure 32). The damping of these modes follows the discussion above: as the modes move radially inwards, i.e., with increasing toroidal mode number, the ion Landau damping increases as the core ion temperatures are higher. At the same time, the mode frequencies increase, i.e., the location

of the TAE gaps (as seen in Figure 25) move to larger frequencies. This actually decreases the ion Landau damping slightly. On the other hand, radiative damping becomes larger for more localised mode structures through its dependence on $k_{\perp}\rho_i$, whereas as modes move into the low shear region, radiative damping decreases for higher n modes. Finally, for $n \approx 20$ the modes become very localised and do not couple through multiple gaps (see Figure 32). There is therefore no interaction with the continuum at the plasma edge ($s \approx 0.85$). For lower mode numbers, continuum damping tends to be higher since the distance between the closed edge continuum and the main TAE gap is reduced and the mode structures are more global. In Figure 34, the dependencies for the modes of Figure 32 are given. It should be noted that in this study only the “main” or “innermost” TAE branch with the dominant poloidal harmonics ($m, m+1$) with $m = n$ was considered. Other branches with the same n but higher m 's can have lower damping for some toroidal mode numbers (as will be reported elsewhere).

Including the α -particle and the NBI drive for these cases results in weakly unstable modes: for $n = 25$, where the drive is more efficient due to $k_{\theta}\Delta_z$ being closer to 1 for higher $|k_{\theta}| \approx m/r$, the growth rate is found to be $\gamma/\omega = 1.1\%$, and for $n = 11$, $\gamma/\omega = 0.07\%$. Since the mode structure for the latter case is already rather extended, it is possible that particles are transported from $s = 0.5$ towards the plasma edge. However, since the energetic particle density is already relatively small at mid-radius, only a small effect on the

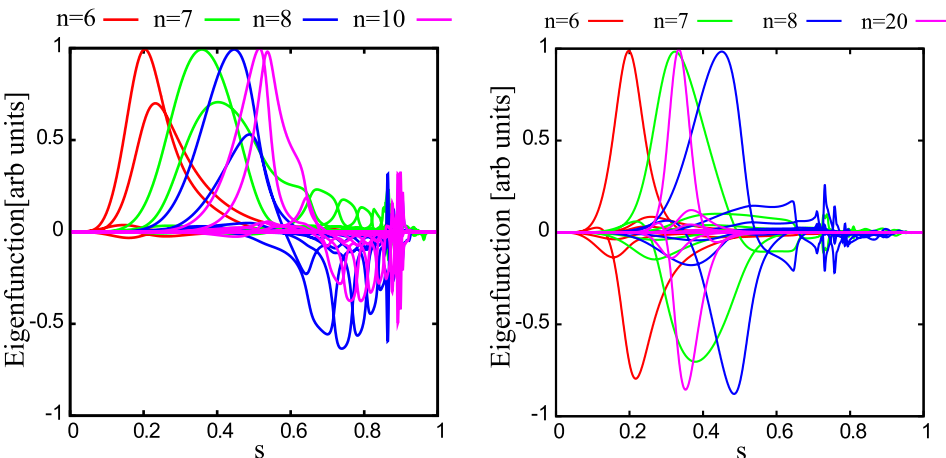


FIG. 33. Left: Eigenfunctions (electrostatic potential) for low- n symmetric TAEs and $q_0 = 0.90$; Right: eigenfunctions (electrostatic potential) for low- n anti-symmetric TAEs and $q_0 = 0.90$.

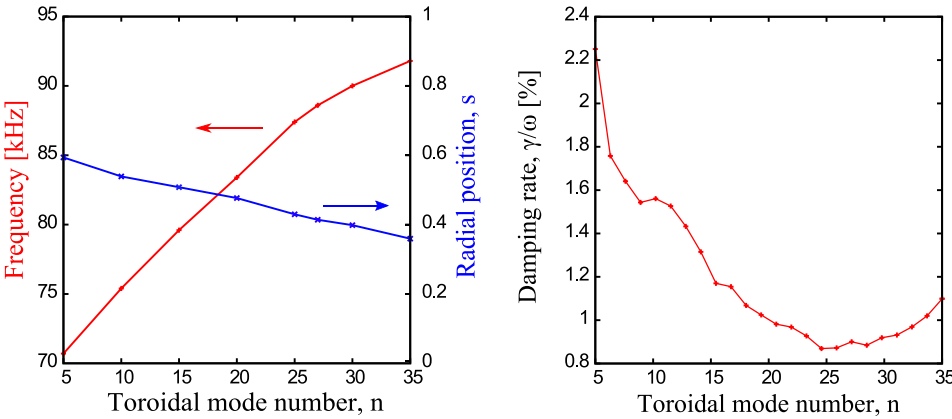


FIG. 34. Left: TAE frequency and radial position as a function of their toroidal mode number ($q_0 = 0.985$); right: Damping as a function of toroidal mode number.

fusion performance would be expected from a quasi-linear estimate. Nevertheless, even a small increase in the energetic particle flux to the first wall is of concern and, therefore, non-linear hybrid simulations will be carried out, on the basis of this stability analysis, in order to understand and quantify possible non-linear effects (“domino effect”) that could considerably increase the energetic particle transport in the outer core region and thus also the wall loads.

In summary, this numerical analysis supports the conclusions drawn from the analytic work described in Secs. III–VIII. Relatively good agreement is found for the reduced local ion Landau damping estimates due to isotope mix effects. The drive due to α -particles and NBI is comparable in magnitude and leads to weakly unstable modes for $s > 0.4$ and $n \sim 15\text{--}30$.

In Secs. X–XII, the influence of energetic ions on other global MHD phenomena is considered.

X. INTERACTION OF ENERGETIC PARTICLES AND SAWTOOTH OSCILLATIONS

The sawtooth instability in tokamak plasmas results in a periodic reorganization of the core plasma. A typical sawtooth cycle consists of a quiescent period, during which the plasma density and temperature increase, followed by the growth of a helical magnetic perturbation, which in turn is followed by a rapid collapse of the central pressure. Sawteeth with long quiescent periods have been observed to result in the early triggering of neo-classical tearing modes (NTMs) at low plasma pressure,⁴⁶ which can, in turn, significantly degrade confinement. It is predicted that fusion-born α particles will lead to very long sawtooth periods in ITER.^{47–49} Indeed, this has been verified empirically as alpha-tail production with ICRF heating of ${}^4\text{He}$ -beam ions in JET confirmed that the energetic alpha particles result in “monster” sawteeth^{50–55}—sawteeth with periods longer than the energy confinement time, and hence saturated central plasma temperature. High power ICRH experiments in JET showed that the sawtooth instability was suppressed for many seconds⁵⁰ and long sawtooth quiescent periods were terminated abruptly by a sawtooth collapse that followed the switch off of the ICRH.⁵¹ As well as stabilising sawteeth, ICRH has also been applied to deliberately destabilise the sawteeth when preferentially propagating waves are

applied.^{56–60} Finally, it was also shown that fusion-born α particles produced a strongly stabilising effect on sawteeth.⁵⁶

This fast ion stabilisation of sawteeth is a concern in ITER since the combination of alphas and energetic particles from auxiliary heating will lead to long sawtooth periods, which are more likely to trigger confinement-degrading NTMs. This stabilisation was attributed to kinetic effects arising from the presence of a population of core energetic trapped ions. The mechanism for the stabilisation of the low-frequency MHD perturbations by trapped fast ions is a result of the conservation of the third adiabatic invariant.⁶¹ Porcelli⁶² proposed that in a tokamak equilibrium, this third adiabatic invariant of motion,⁶³ Φ_{ad} , is equivalent to the flux of the poloidal magnetic field through the area defined by the toroidal precession of the trapped particle orbit centres. In order for Φ_{ad} to be conserved, the time it takes a trapped ion to complete a toroidal orbit must be short compared to the timescale of the mode, $2\pi/\omega$.

The injection of 350 keV negative-ion based neutral beams (N-NBI) in JT-60U also led to strong stabilisation of sawteeth,⁶⁴ despite the fact that the resulting fast ion population was predominantly passing. This led to the hypothesis that circulating ions also influence the $n=1$ internal kink mode stability, which underlies sawtooth oscillations. As described in Refs. 65 and 66, the internal kink is stabilised when $\partial f_{\text{fast}}(v_{||} > 0)/\partial r < \partial f_{\text{fast}}(v_{||} < 0)/\partial r$, which occurs when the energetic ions are injected either off-axis ($\partial f_{\text{fast}}/\partial r > 0$) and oriented opposite to the plasma current, or when the fast ion population is predominantly on-axis ($\partial f_{\text{fast}}/\partial r < 0$) and directed with the plasma current. This effect has been demonstrated by experiments that exhibit an asymmetry in sawtooth behaviour depending upon whether the NBI is injected co- I_p , or counter-current in JET,^{67,68} MAST,⁶⁹ and TEXTOR.⁷⁰ Furthermore, off-axis NBI shortens the sawtooth period due to peaking of the fast ion distribution outside the $q=1$ surface.^{71–73} Following this empirical verification of the influence of passing energetic ions upon the sawtooth behaviour, experiments using ion cyclotron resonance heating with a ${}^3\text{He}$ minority scheme were conducted in JET to demonstrate that effective moderation of the sawtooth behaviour could be achieved by tailoring the energetic ion distribution function, symmetric in the absence of driven current.^{74,75} Figure 35 shows that the sawtooth period can be decreased using ${}^3\text{He}$ minority ICRH symmetric in H-mode

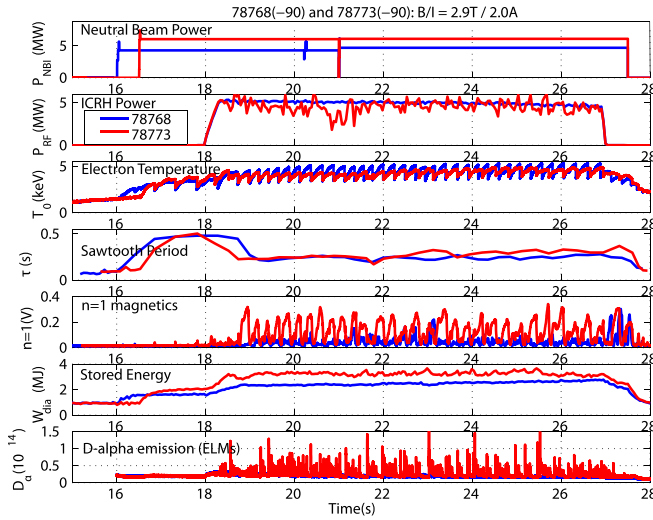


FIG. 35. JET pulse 78 768 (in blue) with 4.8 MW of NBI, and JET pulse 78 773 (in red) with 6.4 MW of NBI, where both employed low concentration ^3He minority ICRH at around 5 MW. In both, the -90° antenna phasing produces counter current propagating waves, which shorten the sawtooth period, shown by τ (s). Also shown is the central electron temperatures in the core, the $n = 1$ magnetic perturbation amplitude, the stored energy W_{dia} , and D_α emission, which indicates that JET pulse 78 773 achieves robust sawtooth control even in high confinement mode. Adapted by permission from Macmillan Publishers Ltd: J. P. Graves, I. T. Chapman, S. Coda, M. Lennholm, M. Albergante and M. Jucker, “Control of magnetohydrodynamic stability by phase space engineering of energetic ions in tokamak plasmas,” Nature Communications, vol. 3, p. 624, 2012, copyright 2012 (Ref. 75).

plasmas. This destabilisation can be attributed solely to the effect of barely passing fast ions since there is negligible change in the local magnetic shear; this has been confirmed with minority concentration scans, which alter the effect of the fast ions by changing the tail temperatures and fast ion fraction, in excellent agreement with numerical modelling.^{66,75} This demonstration means that ICRH could be considered as a sawtooth control actuator in ITER.⁷⁶

Early experiments on JET and TFTR showed that suprathermal ions were expelled from the plasma core by sawtooth oscillations.^{77,78} Soon after, a theory was developed whereby fast ions were redistributed during the crash due to their motion along the evolving flux surfaces, which implied the same mechanism of redistribution of the high energy ions and the particles of the bulk plasma.⁷⁹ In deuterium-tritium plasmas in TFTR, it was observed that sawtooth crashes could result in a very inhomogeneous flux of alpha particles to the wall.⁸⁰ The radial profiles of the density of the confined alpha particles with energies in the range of 0.15 to 0.6 MeV have been measured before and after a sawtooth crash⁸¹ with a large decrease in the core alpha density observed, consistent with theoretical models for suprathermal ion redistribution.^{79,82} Similar redistribution of energetic ions is also observed on JET where measurements from the JET neutron profile monitor have been analyzed topographically to deduce the 2-D spatial distribution of neutron emissivity during NBI heating both before and after sawtooth crashes. In a discharge where the global neutron emission decreases slightly to 5/6 of the pre-crash rate, the axial emissivity drops down to values as low as only 1/6 of the pre-crash value.⁸³ Neutron spectroscopy has also shown that ICRH generated fast

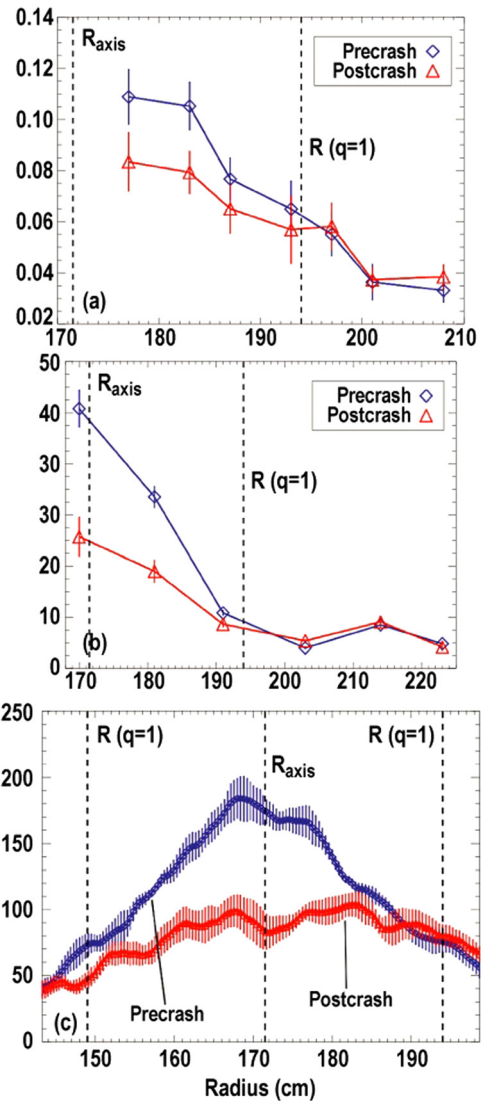


FIG. 36. Radial profiles at the midplane proportional to the fast-ion density just before and just after an average sawtooth crash. The major radii of the magnetic axis and the $q = 1$ surface are denoted. (a) Trapped fast ions (detected by the vertical FIDA system). (b) Co-circulating fast ions (detected by the near-tangential FIDAsystem). (c) Counter-circulating fast ions (detected by the FIDA imaging system). The 1D radial profiles from the imaging system are extracted from pixels that detect signal along the mid-plane. Reprinted with permission from C. M. Muscatello *et al.*, “Velocity-space studies of fast-ion transport at a sawtooth crash in neutral-beam heated plasmas,” Plasma Phys. Controlled Fusion **54**(2), 025 006 (2012). Copyright 2012 IOP Publishing. Reproduced by permission of IOP Publishing. All rights reserved.

ions in the 100 keV range in JET are redistributed by sawteeth,⁸⁴ whilst 1 MeV tritons suffer only modest redistribution at sawtooth crashes.⁸⁵ In other ICRF heated JET discharges, neutron emission spectroscopy has been used to show the behaviour of fast deuterons of various energies throughout the sawtooth cycle, including a reduction of ions with energies in excess of 1.3 MeV and an increase of ions with energies greater than 500 keV due to core-localised TAE (inside the $q = 1$ surface) just prior to a (“monster”) sawtooth crash.⁸⁶

Following development of diagnostics such as imaging of Doppler shifted fast ion D_α light (FIDA) emitted by re-neutralized energetic ions⁸⁷ and collective Thomson scattering,⁸⁸ more accurate information has been obtained about

sawtooth-induced fast ion redistribution. For instance, imaging of FIDA emission during sawtooth events in DIII-D shows a large central depletion following the crash, indicative of a broad redistribution of fast ions. Figure 36 shows that passing fast ions are observed to undergo larger redistribution than their trapped counterparts in DIII-D⁸⁹ as also seen in TEXTOR.⁹⁰ Whilst passing ions of all energies are redistributed, only low-energy trapped ions suffer redistribution during a sawtooth crash, consistent with transport dependent upon the magnitude of toroidal drift. Similarly, the fast-ion distribution measured by collective Thomson scattering and resolved close to perpendicular to the magnetic field showed no clear reduction at the time of a sawtooth crash, whereas at angles far from perpendicular a significant reduction is observed. This indicates that the fast-ion redistribution is either pitch angle or energy dependent or both.⁹¹

Finally, the redistribution of particles caused by a sawtooth crash also has beneficial consequences. For instance, impurity accumulation has been avoided in JET through tailoring of the sawtooth period,⁹² allowing higher confinement. It is thought that frequent small sawtooth crashes in a burning plasma could serve the same purpose by expelling helium ash from the core.^{92–94}

XI. INTERACTION OF ENERGETIC PARTICLES AND NEO-CLASSICAL TEARING MODES

Neo-classical tearing modes are driven by a helical perturbation that reduces the local bootstrap current—a self-generated plasma current in regions of strong pressure gradients and low collisionality. This local reduction in bootstrap current results from the pressure profile flattening in the presence of a magnetic island. NTMs enhance cross-field transport and degrade confinement, sometimes even leading to plasma terminations. It has been observed that NTMs also lead to enhanced fast ion losses.^{5–7} The fast ion losses are modulated at the same frequency as the mode, as illustrated in Figure 37. A detailed analysis of the particle trajectories explains the underlying loss mechanisms through: (i) losses of passing particles caused by drift island formation, and (ii) losses of trapped particles due to stochastic diffusion.^{95,96} However, fast ion orbit modelling in the presence of a 3D perturbation from an NTM suggests that there will be an insignificant change in wall loads due to lost energetic ions in ITER.⁹⁷

It has also been conjectured that energetic particle effects play a role in the stability of NTMs. Recent results from JET show that NTMs are stable in parameter regimes where they are observed to be unstable in other tokamaks.⁹⁸ The most significant difference in the dimensionless parameters of these otherwise similar discharges is β_{fast} , with JET exceeding 30% fast ion fraction, whilst DIII-D and JT-60U are typically below 20%. It has subsequently been shown numerically that energetic particles provide a significant damping effect at experimentally relevant β_{fast} .⁹⁹ Conversely, unstable NTM modes can be driven by energetic particles far into the MHD stable region in (q_{\min}, β_N) space.¹⁰⁰ In both cases, energetic particles are found to modify NTM stability when compared to the MHD-only result. The effects from individual particle species have also been

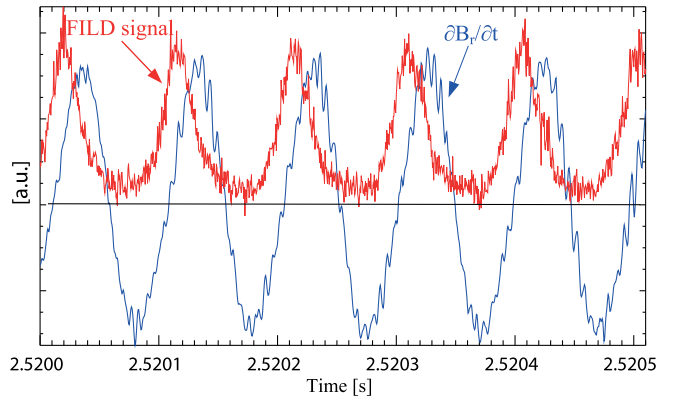


FIG. 37. ASDEX Upgrade discharge #21081: Phase correlation between fast ion losses and the Mirnov signal $\partial B_r / \partial t$ due to the magnetic island. Reprinted with permission from E. Poli *et al.*, “Observation and modeling of fast trapped ion losses due to neoclassical tearing modes,” Phys. Plasmas **15**(3), 032 501 (2008). Copyright 2008 American Institute of Physics.

assessed, and the net effect of trapped energetic particles on tearing modes is much more destabilizing when compared to that of circulating particles at the same β_N value.¹⁰¹

XII. INTERACTION OF ENERGETIC PARTICLES AND RESISTIVE WALL MODES

In this section, we consider the ITER steady-state scenario,^{102,103} which is designed to operate above the no-wall beta limit at 9MA, $\beta_N = 2.9$ and achieve a fusion gain factor $Q = 5$, meaning that the stability and control of the RWM is a significant concern.¹⁰⁴ The safety factor profile is strongly reversed with $q_0 = 2.6$, $q_{\min} = 1.5$, and $q_{95} = 4.8$. The pedestal height is assumed to be 60 kPa and there is no internal transport barrier in the pressure profile. In the absence of a surrounding wall, the plasma is stable to kink modes until the normalised plasma pressure, $\beta = 2\mu_0 < p > / B^2$, exceeds a critical value, β^∞ , the no-wall β -limit. In the presence of an ideally conducting wall, the plasma is stable to a critical value, β^b with the range $\beta^\infty < \beta < \beta^b$ called the

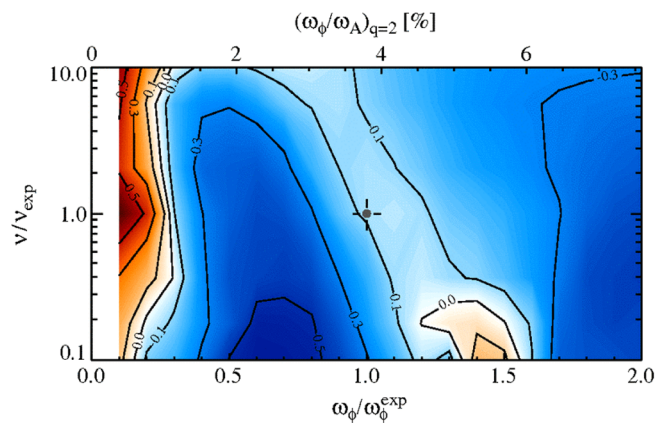


FIG. 38. Contours of the RWM growth/damping rate (shown as $\gamma \tau_w$, where τ_w is the wall time) for various collisionalities and rotation scaled to the experimental case in NSTX. Blue shows stable regions, red unstable. The growth rate is clearly non-monotonic with rotation. Reprinted with permission from J. W. Berkery *et al.*, “Resistive wall mode instability at intermediate plasma rotation,” Phys. Rev. Lett. **104**(3), 035 003 (2010). Copyright 2010 American Physical Society.

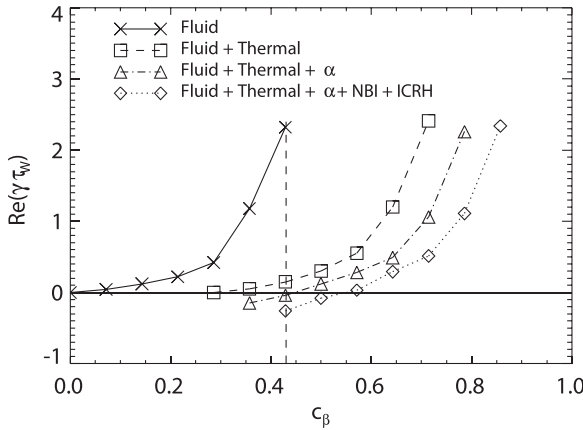


FIG. 39. The growth or damping rate of the RWM in the ITER 9MA steady-state scenario found using the change in the mode potential energy associated with kinetic effects, as a function of $C_\beta = (\beta - \beta_\infty)/(\beta_b - \beta_\infty)$ when only ideal fluid stability is considered or when additional damping from thermal and fast ion populations are considered for a rotation speed at the magnetic axis in ITER of $v = 0.01v_A$.¹²⁹ The marginal stability point is increased significantly by including all these damping effects, only made possible by including finite orbit width effects. The target value of C_β to achieve $Q = 5$ in the ITER 9MA steady-state scenario is $C_\beta = 0.43$ and corresponds to the vertical dashed line. Reprinted with permission from I. T. Chapman *et al.*, “Kinetic damping of resistive wall modes in ITER,” Phys. Plasmas **19**(5), 052 502 (2012). Copyright 2012 American Institute of Physics.

wall-stabilised region. In practice, the vessel wall has a finite resistivity. Thus, on the time scale required for eddy currents to decay resistively, the magnetic perturbation of the external kink mode can penetrate the wall and so wall-stabilisation is lost. A number of tokamaks have operated above the β^∞ -limit,^{105–111} even with very low rotation.^{112,113} Consequently, in order to make reliable extrapolation to ITER, it is crucial to understand the passive stabilisation of the RWM provided by kinetic effects.

Various models have been proposed to explain RWM damping due to kinetic effects, such as sound-wave damping,¹¹⁴ ion Landau damping,¹¹⁵ or damping arising from resonance with the precessional drift of thermal ions.^{116,117} Numerical simulation has subsequently shown that the damping from resonance with the precession frequency of thermal ions^{118–120} or fast ions^{121,122} can significantly improve RWM stability. The importance of the role of fast ions was demonstrated in NSTX, where the stabilisation provided by rotation was carefully balanced against the resonance of the Doppler-shifted mode frequency with fast ion frequencies to explain the somewhat counter-intuitive observation that RWMs were observed to become more stable at lower rotation.¹¹³ Figure 38 shows how the growth rate of the RWM in NSTX varies with rotation, demonstrating that as the rotation increases, RWM stability improves, then degrades before improving once more at high velocity,¹²⁰ dependent upon whether the mode is in resonance with the precession frequency of the bulk ions. Furthermore, experiments designed to deliberately vary the fast ion distribution have also shown a change in the damping of the RWM as measured by the resonant field amplification,^{123,124} again attributed to wave-particle resonances.

The self-consistent inclusion of thermal kinetic effects on RWM stability in generalised toroidal geometry was

assessed in Refs. 125 and 126, before the effects of alpha particles were added and investigated for the ITER 9 MA scenario in Refs. 121 and 122. All of these studies, either with a perturbative or self-consistent treatment of the fast ion interaction with the RWM displacement, find some passive stabilisation of the RWM above the ideal no-wall limit due to the presence of thermal and alpha particles. More recently, even the finite orbit width effects of the energetic particles have been included and shown to provide an important contribution to the stabilising effect of the fast ions.^{75,127,128} Figure 39 shows how the thermal particles, alpha particles, and auxiliary heating-induced energetic particles in the ITER 9MA steady-state scenario all play a role in stabilising the RWM and increasing the effective β -limit.

XIII. FAST PARTICLE LOSSES DUE TO NON-AXISYMMETRIC FIELDS (ELM CONTROL COILS, TEST BLANKET MODULES (TBMS), AND TOROIDAL FIELD (TF) RIPPLE)

In most theoretical analyses of fast particle dynamics for ITER, as for other tokamaks, the magnetic field is assumed to be axisymmetric. However, in reality, this symmetry is never satisfied in any real tokamak. As is well known, the finite number and limited toroidal extent of the TF coils cause a periodic variation of the toroidal field called toroidal magnetic ripple. This ripple can provide a channel for fast particle leakage, leading to very localized heat loads on the plasma-facing components. For ITER, it is desirable that the heat load from the fast ions on the ITER first wall panels is as low as possible (a typical guideline upper value is 0.5 MW/m^2) so that appropriate headroom is available for the first wall panels to handle the thermal loads deposited by the plasma in the same regions as the fast particle loads. The design values for the heat loads of the beryllium first wall panels in ITER are $1\text{--}2 \text{ MW m}^{-2}$ in the low loading areas and 4.7 MW m^{-2} in the high loading areas.¹³⁰ Ferromagnetic Inserts (FIs) with ferromagnetic steel are embedded in the double wall structure of the ITER vacuum vessel in the regions under the TF coils in order to reduce the toroidal field ripple. In ITER, the toroidal field perturbations are further locally increased by the presence of discrete ferromagnetic structures, the TBMs for demonstration of tritium breeding,¹³¹ and the lower smaller amount of ferromagnetic material that can be inserted in the region of the machine where the NBI ports are located. Thus, there are complex toroidal symmetry-breakings in the ITER equilibrium magnetic field configuration, which can lead to localised fast particle losses. In Figure 40, the variation of the toroidal magnetic field and of its ripple at a point near the plasma outer midplane in ITER is shown.¹³² ITER has 18 TF coils, the NBI ports are located within the toroidal angles between 50° and 100° , and the TBMs are installed at three ports around 30° , 310° , and 350° . By installing FIs, the ripple may be reduced by about one third of the one without FIs, as shown in the region between 110° and 290° in Figure 40. In the region where the TBMs are installed, the ripple increases locally to values larger than those of the TF ripple if FIs were absent. The FIs have a poloidally extended distribution

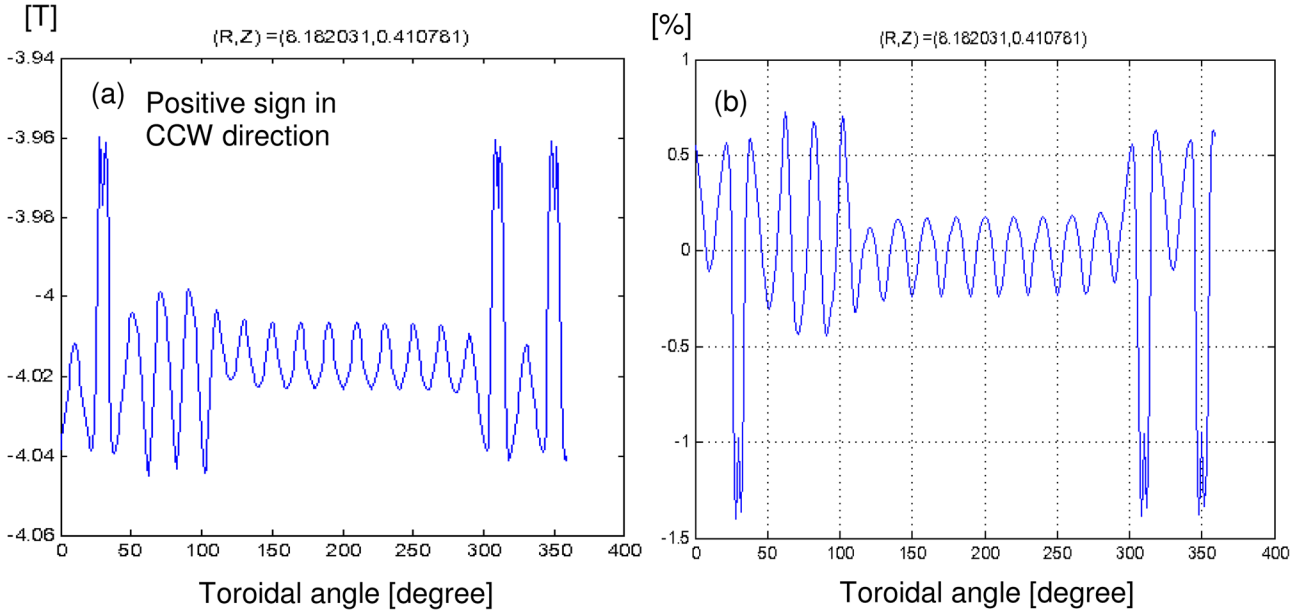


FIG. 40. (a) Toroidal variation of the toroidal magnetic field, B_T . (b) Toroidal variation of the toroidal magnetic field ripple $(B_T - \langle B_T \rangle)/\langle B_T \rangle$ at $(R,Z) = (8.18 \text{ m}, 0.41 \text{ m})$ in ITER.

on the low field side, whereas the TBMs are located at the equatorial ports around the mid-plane. This means that the toroidal field variation shown in Figure 40 changes also in the poloidal direction. The resulting perturbed magnetic field thus has a complicated structure and it is not possible to make a simple analytic field model describing it.

In addition to the toroidal field asymmetries caused by the finiteness of the TF coils and the ferromagnetic elements incorporated in the ITER design, there are additional 3D fields, which are expected to be applied for the purposes of ELM control in ITER scenarios that further perturb the magnetic field structure. An example of such 3-D vacuum field produced by the ITER ELM control coils alone is shown in

Figures 41(a)–41(c).¹³³ The ELM control coils field deforms the field generated by TF coils and FIs as shown in Figures 41(d)–41(f). As can be seen in these figures, the perturbation produced by the ELM control coils is not negligible when compared with the fields generated by the finiteness of the TF coils and the FIs.

There are two important factors causing the transport of fast ions in a non-axisymmetric magnetic field: the first comes from the collisionless behaviour of fast ions and the second from collisional effects with the bulk plasma. For the first, the resonance of a fast-ion trajectory with the perturbed field is necessary. This can be viewed as a “wave-particle interaction” such as that occurs with the field structure from

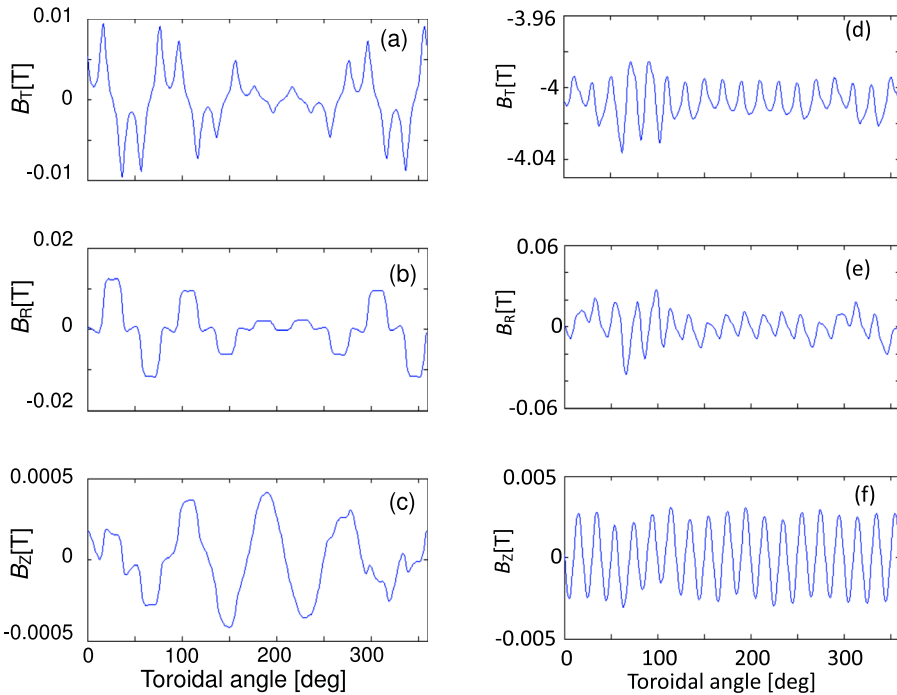


FIG. 41. Magnetic field variation at the position of $(R, Z) = (8.2 \text{ m}, 0.6 \text{ m})$, i.e., near the separatrix outer midplane, for a current in the ELM control coils of 30 kAt. This corresponds to the minimum coil current required to achieve the level of edge magnetic field perturbation to achieve ELM control on the basis of vacuum field estimates for a $n = 4$ cosine waveform and the 15 MA baseline scenario. (a)–(c) are for the field produced solely by the ELM control coils. (d)–(f) are for the field by TF coils + FIs + ELM control coils.

an Alfvén Eigenmode. The resonance induces a drift island in the fast-ion trajectory. In a system in which the perturbation is so large that two adjacent islands overlap, the fast-ion trajectory becomes stochastic and fast ions are transported in a collisionless manner on a very short time.¹³⁴ Even in a system with a small perturbation, collisional effects from the bulk plasma can give rise to additional transport of the fast ions. Fast ions can migrate through the various closed islands in a diffusive manner due to collisions. The prompt loss of fast ions born on unconfined orbits is an additional factor to be considered when it comes to fast ion loss. In reality, fast ions transport and loss is due to a combination of these basic mechanisms.

For a periodic 3D field structure, there are many early analytic works treating fast ion transport.^{134–136} However, they are not suitable to use for ITER predictions or design because the field structure is as complex as mentioned above. In particular, localised heat loads, which are a crucial issue, cannot be estimated analytically. Under these circumstances, orbit following calculations using Monte Carlo methods have been applied to experiments for purposes of studying heat loads and validating the codes^{137,138} in this complicated field structure. The latest validation study was carried out on DIII-D as part of the TBM mock-up project.¹³⁹ Three codes, F3D-OFMC,¹⁴⁰ ASCOT,¹⁴¹ and SPIRAL¹⁴² took part and were validated.

As mentioned above, heat loads on the first wall have been considered to be a crucial issue for the ITER design. Several studies have been carried out as the ITER wall shape and FI design have evolved towards their final design, as well as the development of new plasma scenarios. The two scenarios considered are an inductive 15 MA scenario with a full-bore plasma producing 400 MW of fusion power with a fusion gain $Q=10$ for 400 s, and a steady state 9MA scenario with a weak negative magnetic shear, producing about 300 MW of

fusion power with $Q=5$ for 3000 s. So far, no serious heat loads nor deterioration of alpha particle or beam ion confinement has been reported due to the perturbed field created by the TF coils, FIs, and TBMs.^{143,144} An example for a 9MA scenario with TBMs is presented in Figure 42¹⁴⁴ and shows that whilst the heat load locally peaks around the TBMs, it nevertheless remains at rather low values of less than 50 kW/m^2 . In this scenario, the total energetic ion energy loss rate corresponds to around 0.2% for 70 MW of alpha power production.

The introduction of a further perturbation to the magnetic field in ITER by the ELM control coils has been modelled and shown to lead to a clear deterioration of the NBI ion confinement.^{140,145} In these studies, the vacuum field approximation was used due to the lack of a better representation in which plasma response was considered. The loss power fraction of NB ions reached 7.5% for the case shown in Figure 41, rising to 16.8% if the ELM coil current is increased to 45 kAt,¹⁴⁶ which is much larger than that due to the TF ripple caused by the finiteness of the TF coils alone, which for comparison is 0.8%. Indeed, this large loss fraction has been found to correspond to the field created by the ELM control coils alone as simulations with the ELM control coil field but without any TF ripple show similar NBI loss fractions. These lost NBI ions are preferentially lost to the divertor region leading to peak heat loads of up to 0.27 MW/m^2 for an ELM control current of 30 kAt, as shown by the light green dots in Figure 43. This figure also depicts the origin or birth points of the loss beam ions, which are predominantly lost within 20 ms after entering the plasma and being ionized. The reason why so many NB ions are generated in the edge region is the high density conditions associated with operation of ITER in the 15 MA baseline scenario and this peripheral ionization may be lower if the

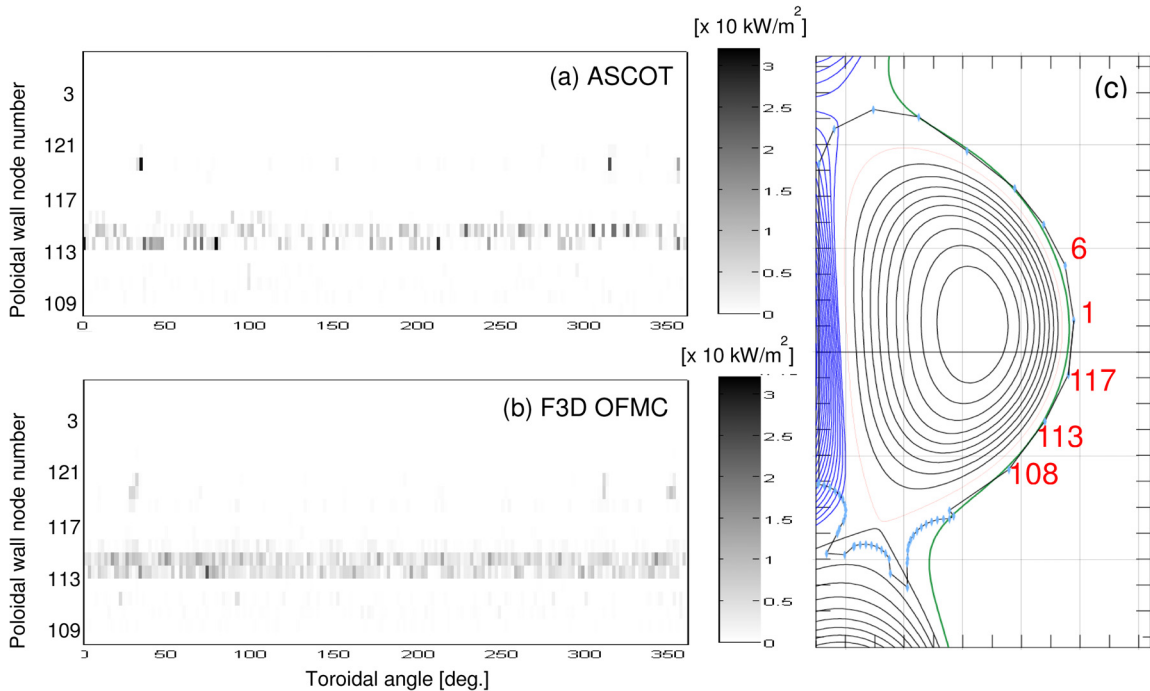


FIG. 42. Heat load distribution for ASCOT (a) and F3D OFMC (b) for the 9 MA $Q=5$ ITER scenario. The horizontal axis is the toroidal angle. The vertical axis is the poloidal wall node number as illustrated in (c). Reprinted with permission from K. Shinohara *et al.*, “Effects of complex symmetry-breakings on alpha particle power loads on first wall structures and equilibrium in ITER,” Nucl. Fusion **51**(6), 063 028 (2011). Copyright 1995 IAEA.

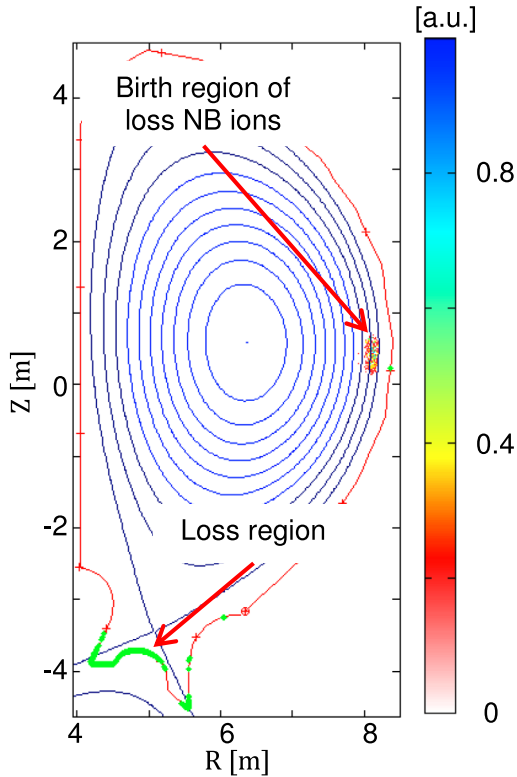


FIG. 43. Origin of lost NB ions and points of impact of lost NB ions.

edge density of the plasma were lower. Due to the wide region of ergodized magnetic field (up to $r/a = 0.6$ for the highest current of 90 kAt in the ELM control coils), which is created by the application of the ELM control coil field, as evaluated in the vacuum approximation, the NBI ions deposited in the peripheral region can be readily lost to the plasma facing components by transport along the field line leading to the large heat loads evaluated in these studies; whether such losses will occur in reality when plasma response is included remains a subject of further studies. Despite these open questions, this study has shown that the transport of fast ions can be increased when the 3D field configuration created by the ELM control coils is optimized for ELM control and maximum edge magnetic field ergodization. This result highlights the importance of performing calculations in which the effects of the non-axisymmetric components of the equilibrium magnetic field are self-consistently taken into account to evaluate fast particle losses in the real magnetic field configuration of fusion devices.

Calculations of fast ion redistribution, loss, and the associated wall loadings taking into account the plasma's response to 3D field perturbations are just beginning. Early reports of calculations including plasma response effects and validated by fast ion loss detector (FILD) measurements in DIII-D L-mode plasmas are however promising.¹⁴⁷ Initial evaluations for ITER show that the inclusion of the shielding of the ELM control coil field by the plasma can reduce significantly the loss of NBI ions¹⁴⁸ with respect to the evaluations done in the vacuum approximation above, which is in agreement with the significant reduction of the width of the ergodized edge magnetic field region when plasma shielding is included.¹⁴⁹ The question remains open to which level the applied vacuum field

by the ELM control coils will be shielded or amplified at the plasma edge by the plasma's response in ITER.

In conclusion for this section, it was previously suspected that 3D deformations of the plasma equilibrium could lead to an additional mechanism for fusion alphas to leak out at unacceptable levels. However, for the levels of TF ripple foreseen in ITER (including FIs and TBMs) and the magnetic field perturbation expected to be applied for ELM control purposes, the 3D deformation of the plasma equilibrium has proven to be so small that the effect on the confinement of fast ions in the core plasma region is negligible.^{144,150,151}

Losses from the plasma edge associated with the use of the ELM control coils are, however, found to be higher, with beam power loss fractions of up to 16.8% reported¹⁴⁶ for ELM control coil currents of 45 kAt (albeit using a vacuum approximation to describe the resulting perturbed field). This motivates future work including a more self-consistent treatment of the plasma equilibrium and background parameters in this region including the response of the plasma to the externally applied 3D fields.

XIV. SUMMARY

This paper has described the consistent picture that has arisen from careful analytic and numerical considerations of the Alfvén Eigenmode stability in the 15 MA ITER baseline scenario. Analytic estimates show that only in the outer region of the plasma ($r/a > 0.5$) is the density of Alfvén continuum gaps high enough to produce global TAE modes (i.e., modes with many poloidal harmonics, coupled due to continuum gaps located at a wide range of radial positions). Despite relatively low alpha-particle and beam ion populations in this part of the plasma, it is only here that the fast particle drive is expected to exceed the ion Landau damping rate, giving a net drive of $\gamma/\omega \sim 0.15\%$. Additionally, because the population of alpha-particles in this external region is relatively low, any TAE-induced redistribution is not expected to influence the burn process. The loss of NBI ions from this peripheral region, on the contrary, maybe more significant as their deposition is more uniformly distributed across the minor radius. Therefore, energetic ion losses to the first wall by TAE remain an open issue, which should be investigated with nonlinear hybrid models. The analytic results presented in this paper are supported by detailed numerical analysis using the gyrokinetic linear stability code, LIGKA, which also found weakly unstable modes for $s > 0.4$ and $n \sim 15-30$.

It should be remarked that the AE stability analysis presented in this paper has focused upon the flat-top phase of the 15 MA ITER baseline scenario. In the future, a full analysis should be performed in which the path to this operation point is evaluated, both within a single discharge, but also as part of the broader development of the ITER Research Plan in which discharges are initially foreseen to be run at reduced field and current. Since the thermal ion Landau damping of TAE is exponentially sensitive to the ion temperature (see Figure 18), this implies that plasmas with $T_i \leq 15$ keV could be more unstable to TAE than the $Q = 10$ operational point itself, something that warrants further

investigation. Indeed, the methods used to heat the plasma to the desired temperature should be investigated in detail for the whole operational path towards $Q = 10$.

In addition to the ability of energetic ions to drive Alfvén Eigenmodes, this paper has also reviewed their influence upon other global MHD phenomena expected in ITER's primary operating scenarios: sawteeth, NTMs, and RWMS.

Fast ion losses due to the non-axisymmetric fields arising from the finite number of toroidal field coils, the inclusion of ferromagnetic inserts, the presence of TBMs with ferromagnetic material, and the field created by the ELM control coils in ITER have been reviewed. The largest source of losses and associated heat loads onto plasma facing components comes from NBI ions in the presence of the ELM control coils with an optimized current configuration for ELM control. In this case, the lost NBI ions were born near the periphery of the plasma and lost to the plasma facing components along the ergodized magnetic field (evaluated in the vacuum approximation). This motivates future work including a more self-consistent treatment of the plasma equilibrium and background parameters in this region including the response of the plasma to the externally applied 3D fields.

Not covered in this paper are the potential synergistic effects that can arise from the simultaneous occurrence of the described phenomena. For example: (i) the redistribution of fast ions from within the $q = 1$ surface to outside by core-localised TAE during a sawtooth cycle and the resulting influence on the $n = 1$ internal kink's stability; (ii) the influence of applying a 3D ELM control coil field on the spectrum and stability of AE in the outer region of the plasma and its effect on the localisation of any associated fast ion losses.

ACKNOWLEDGMENTS

This project has received funding from the European Union's Horizon 2020 research and innovation programme under Grant Agreement No. 633053 and from the RCUK Energy Programme [Grant No. EP/I501045]. The views and opinions expressed herein do not necessarily reflect those of the European Commission or the ITER Organization.

¹ITER Physics Expert Group on Energetic Particles, ITER Physics Expert Group on Heating and Current Drive and ITER Physics Basis Editors, "ITER Physics Basis, Chapter 5," *Nucl. Fusion* **39**, 2471 (1999).

²A. Fasoli, C. B. H. L. Gormenzano, B. N. Breizman, S. Briguglio, D. S. Darrow, N. Gorelenkov, W. W. Heidbrink, A. Jaun, S. V. Konovalov *et al.*, "Progress in the ITER Physics Basis, Chapter 5," *Nucl. Fusion* **47**, S264 (2007).

³S. E. Sharapov, B. Alper, H. L. Berk, D. N. Borba, B. N. Breizman, C. D. Challis, I. G. J. Classen, E. M. Edlund, J. Eriksson, A. Fasoli *et al.*, "Energetic particle instabilities in fusion plasmas," *Nucl. Fusion* **53**(10), 104022 (2013).

⁴N. N. Gorelenkov, S. D. Pinches, and K. Toi, "Energetic particle physics in fusion research in preparation for burning plasma experiments," *Nucl. Fusion* **54**(12), 125001 (2014).

⁵E. Poli, M. I García-Muñoz, H.-U. Fahrbach, S. Günter, and ASDEX Upgrade Team, "Observation and modeling of fast trapped ion losses due to neoclassical tearing modes," *Phys. Plasmas* **15**(3), 032501 (2008).

⁶M. García-Muñoz, P. Martin, H.-U. Fahrbach, M. Gobbin, S. Günter, M. Maraschek, L. Marrelli, H. Zohm, and ASDEX Upgrade Team, "NTM induced fast ion losses in ASDEX Upgrade," *Nucl. Fusion* **47**(7), L10 (2007).

⁷S. Günter, G. Conway, S. daGraça, H.-U. Fahrbach, C. Forest, M. García-Muñoz, T. Hauff, J. Hobirk, V. Iguchine, F. Jenko *et al.*, "Interaction of energetic particles with large and small scale instabilities," *Nucl. Fusion* **47**(8), 920 (2007).

⁸A. R. Polovoĭ, S. Y. Medvedev, V. S. Mukhovatov, A. S. Kukushkin, Y. Murakami, M. Shimada, and A. A. Ivanov, "ITER confinement and stability modelling," *J. Plasma Fusion Res.* **5**, 82–87 (2002).

⁹F. M. Levinton, L. Zakharov, S. H. Batha, J. Manickam, and M. C. Zarnstorff, "Stabilization and onset of sawteeth in TFR," *Phys. Rev. Lett.* **72**(18), 2895–2898 (1994).

¹⁰G. Y. Fu and J. W. Van Dam, "Excitation of the toroidicity-induced shear Alfvén eigenmode by fusion alpha particles in an ignited tokamak," *Phys. Fluids B* **1**(10), 1949 (1989).

¹¹R. Betti and J. P. Freidberg, "Ellipticity induced Alfvén eigenmodes," *Phys. Fluids B* **3**(8), 1865 (1991).

¹²B. N. Breizman and S. E. Sharapov, "Energetic particle drive for toroidicity-induced Alfvén eigenmodes and kinetic toroidicity-induced Alfvén eigenmodes in a low-shear tokamak," *Plasma Phys. Controlled Fusion* **37**(10), 1057 (1995).

¹³G. Y. Fu, "Existence of core localized toroidicity-induced Alfvén eigenmode," *Phys. Plasmas* **2**(4), 1029 (1995).

¹⁴J. Candy, B. N. Breizman, J. W. Van Dam, and T. Ozeki, "Multiplicity of low-shear toroidal Alfvén eigenmodes," *Phys. Lett. A* **215**(5–6), 299 (1996).

¹⁵H. L. Berk, J. W. Van Dam, D. Borba, J. Candy, G. T. A. Huysmans, and S. E. Sharapov, "More on core-localized toroidal Alfvén eigenmodes," *Phys. Plasmas* **2**(9), 3401 (1995).

¹⁶S. Poedts and E. Schwarz, "Computation of the ideal-MHD continuous spectrum in axisymmetric plasmas," *J. Comput. Phys.* **105**(1), 165 (1993).

¹⁷A. B. Mikhailovskii, G. T. A. Huysmans, W. Kerner, and S. E. Sharapov, "Optimization of computational MHD normal-mode analysis for tokamaks," *Plasma Phys. Rep.* **23**(10), 844 (1997).

¹⁸R. Nyqvist and S. E. Sharapov, "Asymmetric radiative damping of low shear toroidal Alfvén eigenmodes," *Phys. Plasmas* **19**(8), 082517 (2013).

¹⁹T. Gassner, K. Schoepf, S. E. Sharapov, V. G. Kiptily, S. D. Pinches, C. Hellesen, J. Eriksson, and JET-EFDA contributors, "Deuterium beam acceleration with 3rd harmonic ion cyclotron resonance heating in Joint European Torus: Sawtooth stabilization and Alfvén eigenmodes," *Phys. Plasmas* **19**(3), 032115 (2012).

²⁰S. E. Sharapov and A. B. Mikhailovskii, in 5th IAEA Technical Meeting on Energetic Particles, JET, Abingdon, UK, 1997.

²¹I. G. Abel, B. N. Breizman, S. E. Sharapov, and JET-EFDA Contributors, "Resonant excitation of shear Alfvén perturbations by trapped energetic ions in a tokamak," *Phys. Plasmas* **16**(10), 102506 (2009).

²²F. Zonca and L. Chen, "Destabilization of energetic particle modes by localized particle sources," *Phys. Plasmas* **7**(11), 4600 (2000).

²³R. Betti and J. P. Freidberg, "Stability of Alfvén gap modes in burning plasmas," *Phys. Fluids B* **4**(6), 1465 (1992).

²⁴J. W. Connor, R. O. Dendy, R. J. Hastie, D. Borba, G. Huysmans, W. Kerner, and S. Sharapov, "Non-ideal effects on toroidal alfvén eigenmode stability," in 21st EPS Conference, Montpellier, 1994.

²⁵N. N. Gorelenkov and S. E. Sharapov, "On the collisional damping of TAE-modes on trapped electrons in tokamaks," *Phys. Scr.* **45**(2), 163 (1992).

²⁶R. R. Mett and S. M. Mahajan, "Kinetic theory of toroidicity-induced Alfvén eigenmodes," *Phys. Fluids B* **4**(9), 2885 (1992).

²⁷J. Candy and M. N. Rosenbluth, "Continuum damping of high-mode-number toroidal Alfvén waves," *Plasma Phys. Controlled Fusion* **35**(8), 957 (1993).

²⁸M. N. Rosenbluth, H. L. Berk, J. W. Van Dam, and D. M. Lindberg, "Continuum damping of high-mode-number toroidal Alfvén waves," *Phys. Rev. Lett.* **68**(5), 596 (1992).

²⁹F. Zonca and L. Chen, "Resonant damping of toroidicity-induced shear-Alfvén eigenmodes in tokamaks," *Phys. Rev. Lett.* **68**(5), 592 (1992).

³⁰P. Lauber, "Linear gyrokinetic description of fast particle effects on the MHD stability in tokamaks," Ph.D. thesis (TU München, 2003).

³¹P. Lauber, S. Günter, A. Könies, and S. D. Pinches, "LIGKA: A linear gyrokinetic code for the description of background kinetic and fast

- particle effects on the MHD stability in tokamaks," *J. Comput. Phys.* **226**(1), 447–465 (2007).
- ³²P. Lauber, S. Günter, and S. D. Pinches, "Kinetic properties of shear Alfvén eigenmodes in tokamak plasmas," *Phys. Plasmas* **12**(12), 122501 (2005).
- ³³F. Zonca, L. Chen, and R. A. Santoro, "Kinetic theory of low-frequency Alfvén modes in tokamaks," *Plasma Phys. Controlled Fusion* **38**(11), 2011–2028 (1996).
- ³⁴F. Zonca, L. Chen, A. Botrugno, P. Buratti, A. Cardinale, R. Cesario, and V. P. Ridolfini, "High-frequency fishbones at JET: theoretical interpretation of experimental observations," *Nucl. Fusion* **49**, 085009 (2009).
- ³⁵P. Lauber, M. Brüdgam, D. Curran, V. Igochine, K. Sassenberg, S. Günter, M. Maraschek, M. García-Muñoz, N. Hicks, and the ASDEX Upgrade Team, "Kinetic Alfvén eigenmodes at ASDEX Upgrade," *Plasma Phys. Controlled Fusion* **51**, 124009 (2009).
- ³⁶P. Lauber, "Super-thermal particles in hot plasmas: kinetic models, numerical solution strategies, and comparison to tokamak experiments," *Phys. Rep.* **533**(2), 33–68 (2013).
- ³⁷G. Y. Fu and J. W. Van Dam, "Stability of the global Alfvén eigenmode in the presence of fusion alpha particles in an ignited tokamak plasma," *Phys. Fluids B* **1**(12), 2404 (1989).
- ³⁸J. Candy and M. N. Rosenbluth, "Nonideal theory of toroidal Alfvén eigenmodes," *Phys. Plasmas* **1**(2), 356–372 (1994).
- ³⁹Z. Gao, L. Peng, P. Wang, J. Dong, and H. Sanuki, "Plasma elongation effects on temperature gradient driven instabilities and geodesic acoustic modes," *Nucl. Fusion* **49**(4), 045014 (2009).
- ⁴⁰I. Chavdarovski and F. Zonca, "Effects of trapped particle dynamics on the structures of a low-frequency shear Alfvén continuous spectrum," *Plasma Phys. Controlled Fusion* **51**(11), 115001 (2009).
- ⁴¹P. Lauber, I. G. Classen, D. Curran, V. Igochine, B. Geiger, S. da Graca, M. García-Muñoz, M. Maraschek, P. McCarthy, and the ASDEX Upgrade Team, "NBI-driven Alfvénic modes at ASDEX Upgrade," *Nucl. Fusion* **52**(9), 094007 (2012).
- ⁴²M. Schneller, P. Lauber, M. Brüdgam, S. D. Pinches, and S. Günter, "Double-resonant fast particle-wave interaction," *Nucl. Fusion* **52**(10), 103019 (2012).
- ⁴³S. D. Pinches, "Nonlinear interaction of fast particles with Alfvén waves in tokamaks," Ph.D. thesis (The University of Nottingham, UK, 1996).
- ⁴⁴S. D. Pinches, L. C. Appel, J. Candy, S. E. Sharapov, H. L. Berk, D. Borba, B. N. Breizman, T. C. Hender, K. I. Hopcraft, G. T. A. Huysmans, and W. Kerner, "Nonlinear interaction of fast particles with Alfvén waves in tokamaks," *Comput. Phys. Commun.* **111**(1–3), 133–149 (1998).
- ⁴⁵S. D. Pinches, V. G. Kiptily, S. E. Sharapov, D. S. Darrow, L.-G. Eriksson, H.-U. Fahrbach, M. García-Muñoz, M. Reich, E. Strumberger, A. Werner, the ASDEX Upgrade Team and JET-EFDA Contributors, "Observation and modelling of fast ion loss in JET and ASDEX Upgrade," *Nucl. Fusion* **46**(10), S904–S910 (2006).
- ⁴⁶I. T. Chapman, R. J. Buttery, S. Coda, S. Gerhardt, J. P. Graves, D. F. Howell, A. Isayama, R. J. La Haye, Y. Liu, P. Maget *et al.*, "Empirical scaling of sawtooth period for onset of neoclassical tearing modes," *Nucl. Fusion* **50**(10), 102001 (2010).
- ⁴⁷B. Hu, R. Betti, and J. Manickam, "Kinetic stability of the internal kink mode in ITER," *Phys. Plasmas* **13**(11), 112505 (2006).
- ⁴⁸F. Porcelli, D. Boucher, and M. N. Rosenbluth, "Model for the sawtooth period and amplitude," *Plasma Phys. Controlled Fusion* **38**(12), 2163 (1996).
- ⁴⁹I. T. Chapman, S. D. Pinches, J. P. Graves, R. J. Akers, L. C. A. Appel, R. V. Budny, S. Coda, N. J. Conway, M. de Bock, L.-G. Eriksson *et al.*, "The physics of sawtooth stabilization," *Plasma Phys. Controlled Fusion* **49**(12B), B385 (2007).
- ⁵⁰D. J. Campbell, D. F. H. Start, J. A. Wesson, D. V. Bartlett, V. P. Bhatnagar, M. Bures, J. G. Cordey, G. A. Cottrell, P. A. Dupperex, A. W. Edwards *et al.*, "Stabilization of sawteeth with additional heating in the JET tokamak," *Phys. Rev. Lett.* **60**(21), 2148 (1988).
- ⁵¹C. K. Philipps, J. Hosea, E. Marmar, M. W. Phillips, J. Snipes, J. Stevens, J. Terry, J. R. Wilson, M. Bell, M. Bitter *et al.*, "Ion cyclotron range of frequencies stabilization of sawteeth on Tokamak Fusion Test Reactor," *Phys. Fluids B* **4**(7), 2155 (1992).
- ⁵²M. J. Mantinen, M.-L. Mayoral, V. G. Kiptily, S. E. Sharapov, B. Alper, A. Bickley, M. de Baar, L.-G. Eriksson, A. Gondhalekar, T. Hellsten *et al.*, "Alpha-tail production with ion-cyclotron-resonance heating of $\frac{4}{3}$ He-beam ions in JET plasmas," *Phys. Rev. Lett.* **88**(10), 105002 (2002).
- ⁵³M. L. Mayoral, R. J. Buttery, T. T. C. Jones, V. G. Kiptily, S. E. Sharapov, M. J. Mantinen, S. Coda, O. Sauter, L.-G. Eriksson, F. Nguyen *et al.*, "Studies of burning plasma physics in the Joint European Torus," *Phys. Plasmas* **11**(5), 2607 (2004).
- ⁵⁴J. Jacquinot, H. Altmann, R. J. Anderson, J. Arbez, W. Bailey, D. V. Bartlett, B. Beaumont, G. Beaumont, K. Behringer, P. Bertoldi *et al.*, "Radiofrequency heating on JET," in *Plasma Physics and Controlled Nuclear Fusion Research*, Kyoto, Japan, 1986.
- ⁵⁵D. Start *et al.*, in *29th Annual Meeting of APS Division of Plasma Physics*, San Diego, 1987.
- ⁵⁶M. F. F. Nave, N. N. Gorelenkov, K. G. McClements, S. J. Allfrey, B. Balet, D. N. Borba, P. J. Lomas, J. Manickam, T. T. C. Jones, and P. R. Thomas, "Fast particle effects on the sawtooth stability of JET DT discharges," *Nucl. Fusion* **42**(3), 281 (2002).
- ⁵⁷O. Sauter, E. Westerhof, M. L. Mayoral, B. Alper, P. A. Belo, R. J. Buttery, A. Gondhalekar, T. Hellsten, T. C. Hender, D. F. Howell *et al.*, "Control of neoclassical tearing modes by sawtooth control," *Phys. Rev. Lett.* **88**(10), 105001 (2002).
- ⁵⁸E. Westerhof, O. Sauter, M. L. Mayoral, D. F. Howell, M. J. Mantinen, M. F. F. Nave, B. Alper, C. Angioni, P. Belo, R. J. Buttery *et al.*, "Control of sawteeth and triggering of NTMs with ion cyclotron resonance frequency waves in JET," *Nucl. Fusion* **42**(11), 1324 (2002).
- ⁵⁹L.-G. Eriksson, A. Mueck, O. Sauter, S. Coda, M. J. Mantinen, M.-L. Mayoral, E. Westerhof, R. J. Buttery, D. McDonald, T. Johnson, J.-M. Noterdaeme, and P. de Vries, "Destabilization of fast-ion-induced long sawteeth by localized current drive in the JET tokamak," *Phys. Rev. Lett.* **92**(23), 235004 (2004).
- ⁶⁰L.-G. Eriksson, T. Johnson, M.-L. Mayoral, S. Coda, O. Sauter, R. J. Buttery, D. McDonald, T. Hellsten, M. J. Mantinen, A. Mueck *et al.*, "On ion cyclotron current drive for sawtooth control," *Nucl. Fusion* **46**(10), S951 (2006).
- ⁶¹J. W. Van Dam, M. N. Rosenbluth, and Y. C. Lee, "A generalized kinetic energy principle," *Phys. Fluids* **25**(8), 1349 (1982).
- ⁶²F. Porcelli, "Fast particle stabilisation," *Plasma Phys. Controlled Fusion* **33**(13), 1601 (1991).
- ⁶³T. Northrop and E. Teller, "Stability of the adiabatic motion of charged particles in the Earth's field," *Phys. Rev.* **117**(1), 215 (1960).
- ⁶⁴G. Kramer, M. Iwase, Y. Kusama, A. Morioka, M. Nemoto, T. Nishitani, K. Shinohara, S. Takeji, K. Tobita, T. Ozeki *et al.*, "Fast particle experiments in JT-60U," *Nucl. Fusion* **40**(7), 1383 (2000).
- ⁶⁵J. P. Graves, "Influence of asymmetric energetic ion distributions on sawtooth stabilization," *Phys. Rev. Lett.* **92**(18), 185003 (2004).
- ⁶⁶J. P. Graves, I. Chapman, S. Coda, L.-G. Eriksson, and T. Johnson, "Sawtooth-control mechanism using toroidally propagating ion-cyclotron-resonance waves in tokamaks," *Phys. Rev. Lett.* **102**(6), 065005 (2009).
- ⁶⁷M. F. F. Nave, H. R. Koslowski, S. Coda, J. P. Graves, M. Brix, R. J. Buttery, C. Challis, C. Giroud, M. Stamp, P. de Vries *et al.*, "Exploring a small sawtooth regime in Joint European Torus plasmas with counterinjected neutral beams," *Phys. Plasmas* **13**(1), 014503 (2006).
- ⁶⁸I. T. Chapman, S. D. Pinches, L. C. Appel, R. J. Hastie, T. C. Hender, S. Saarelma, S. E. Sharapov, I. Voitsekhovitch, and J. P. Graves, "Modeling sawtooth stabilization by energetic ions from neutral beam injection," *Phys. Plasmas* **14**(7), 070703 (2007).
- ⁶⁹I. T. Chapman, T. C. Hender, S. Saarelma, S. E. Sharapov, R. J. Akers, N. J. Conway, and the MAST Team, "The effect of toroidal plasma rotation on sawteeth in MAST," *Nucl. Fusion* **46**(12), 1009 (2006).
- ⁷⁰I. T. Chapman, S. D. Pinches, H. R. Koslowski, Y. Liang, A. Krämer-Flecken, the TEXTOR Team, and M. de Bock, "Sawtooth stability in neutral beam heated plasmas in TEXTOR," *Nucl. Fusion* **48**(3), 035004 (2008).
- ⁷¹I. T. Chapman, I. Jenkins, R. V. Budny, J. P. Graves, S. D. Pinches, S. Saarelma, and JET EFDA Contributors, "Sawtooth control using off-axis NBI," *Plasma Phys. Controlled Fusion* **50**(4), 045006 (2008).
- ⁷²I. T. Chapman, V. G. Igochine, J. P. Graves, J. P. Pinches, A. Gude, I. Jenkins, M. Maraschek, G. Tardini, the ASDEX Upgrade Team, and JET EFDA Contributors, "Sawtooth control and the interaction of energetic particles," *Nucl. Fusion* **49**(3), 035006 (2009).
- ⁷³I. T. Chapman, M. F. de Bock, S. D. Pinches, M. R. Turnianski, MAST Team, V. G. Igochine, M. Maraschek, G. Tardini, and ASDEX Upgrade Team, "The effect of off-axis neutral beam injection on sawtooth stability in ASDEX Upgrade and Mega-Ampere Spherical Tokamak," *Phys. Plasmas* **16**(7), 072506 (2009).

- ⁷⁴J. P. Graves, I. T. Chapman, S. Coda, T. Johnson, M. Lennholm, B. Alper, M. de Baar, K. Crombe, L.-G. Eriksson, R. Felton *et al.*, “Experimental verification of sawtooth control by energetic particles in ion cyclotron resonance heated JET tokamak plasmas,” *Nucl. Fusion* **50**(5), 052002 (2010).
- ⁷⁵J. P. Graves, I. T. Chapman, S. Coda, M. Lennholm, M. Albergante, and M. Jucker, “Control of magnetohydrodynamic stability by phase space engineering of energetic ions in tokamak plasmas,” *Nat. Commun.* **3**, 624 (2012).
- ⁷⁶I. T. Chapman, J. P. Graves, T. Johnson, O. Asunta, P. Bonoli, M. Choi, E. F. Jaeger, M. Jucker, and O. Sauter, “Sawtooth control in ITER using ion cyclotron resonance heating,” *Plasma Phys. Controlled Fusion* **53**(12), 124003 (2011).
- ⁷⁷G. J. Sadler, S. W. Conroy, O. N. Jarvis, P. van Belle, J. M. Adams, and M. A. Hone, “Investigations of fast-particle behavior in joint European torus plasmas using nuclear techniques,” *Fusion Sci. Technol.* **18**(4), 556 (1990).
- ⁷⁸S. J. Zweber, J. D. Strachan, R. Boivin, C. W. Barnes, A. Cavallo, E. D. Fredrickson, K. McGuire, H. E. Mynick, and R. B. White, “Escaping 1 MeV Tritons in TFTR,” in 16th European Conference on Controlled Fusion and Plasma Physics, Venice, Italy, 1989.
- ⁷⁹Y. I. Kolesnichenko, Y. V. Yakovenko, D. Anderson, M. Lisak, and F. Wising, “Sawtooth oscillations with the central safety factor, $\{q\}_{0}$, below unity,” *Phys. Rev. Lett.* **68**(26), 3881 (1992).
- ⁸⁰D. J. Grove and D. M. Meade, “Initial studies of confinement, adiabatic compression, and neutral-beam heating in TFTR,” *Nucl. Fusion* **25**(9), 1167 (1985).
- ⁸¹B. C. Stratton, R. J. Ponck, G. R. McKee, R. V. Budny, Z. Chang, F. Wising, and A. Ödblom, “Observation of sawtooth redistribution of non-thermal, confined alpha particles in TFTR DT discharges,” *Nucl. Fusion* **36**(11), 1586 (1996).
- ⁸²Y. I. Kolesnichenko and Y. V. Yakovenko, “Sawtooth oscillations and fast-ion ejection in tokamaks,” *Nucl. Fusion* **32**(3), 449 (1992).
- ⁸³F. B. Marcus, J. M. Adams, A. D. Cheetham, S. Conroy, W. G. F. Core, O. N. Jarvis, M. J. Loughlin, M. Olsson, G. Sadler, P. Smeulders, P. Van Belle, and N. Watkins, “JET neutron emission profiles and fast ion redistribution during sawtooth crashes,” *Plasma Phys. Controlled Fusion* **33**(4), 277 (1991).
- ⁸⁴D. F. H. Start, J. Jacquinot, V. Bergeaud, V. P. Bhatnagar, G. A. Cottrell, S. Clement, L.-G. Eriksson, A. Fasoli, A. Gondhalekar, C. Gormezano *et al.*, “D-T Fusion with ion cyclotron resonance heating in the JET tokamak,” *Phys. Rev. Lett.* **80**(21), 4681 (1998).
- ⁸⁵F. B. Marcus, J. M. Adams, D. S. Bond, M. A. Hone, P. J. A. Howarth, O. N. Jarvis, M. J. Loughlin, G. J. Sadler, P. Van Belle, and N. Watkins, “Effects of sawtooth crashes on beam ions and fusion product tritons in JET,” *Nucl. Fusion* **34**(5), 687 (1994).
- ⁸⁶C. Hellesen, M. Gatou Johnson, E. Andersson Sundén, S. Conroy, G. Ericsson, J. Eriksson, G. Gorini, T. Johnson, V. G. Kiptily, S. D. Pinches *et al.*, “Measurements of fast ions and their interactions with MHD activity using neutron emission spectroscopy,” *Nucl. Fusion* **50**(8), 084006 (2010).
- ⁸⁷W. W. Heidbrink, K. H. Burrell, Y. Luo, N. A. Pablant, and E. Ruskov, “Hydrogenic fast-ion diagnostic using Balmer-alpha light,” *Plasma Phys. Controlled Fusion* **46**(12), 1855 (2004).
- ⁸⁸H. Bindslev, J. A. Hoekzema, J. Egedal, J. A. Fessey, T. P. Hughes, and J. S. Machuzak, “Fast-ion velocity distributions in JET measured by collective thomson scattering,” *Phys. Rev. Lett.* **83**(16), 3206 (1999).
- ⁸⁹C. M. Muscatello, W. W. Heidbrink, Y. I. Kolesnichenko, V. V. Lutsenko, M. A. Van Zeeland, and Y. V. Yakovenko, “Velocity-space studies of fast-ion transport at a sawtooth crash in neutral-beam heated plasmas,” *Plasma Phys. Controlled Fusion* **54**(2), 025006 (2012).
- ⁹⁰S. K. Nielsen, M. Salewski, H. Bindslev, A. Bürger, V. Furtula, M. Kantor, S. B. Korsholm, H. R. Koslowski, A. Krämer-Flecken, F. Leipold *et al.*, “Dynamics of fast ions during sawtooth oscillations in the TEXTOR tokamak measured by collective Thomson scattering,” *Nucl. Fusion* **51**(6), 063014 (2011).
- ⁹¹S. K. Nielsen, H. Bindslev, M. Salewski, A. Bürger, E. Delabie, V. Furtula, M. Kantor, S. B. Korsholm, F. Leipold, F. Meo *et al.*, “Fast-ion redistribution due to sawtooth crash in the TEXTOR tokamak measured by collective Thomson scattering,” *Plasma Phys. Controlled Fusion* **52**(9), 092001 (2010).
- ⁹²M. F. F. Nave, J. Rapp, T. Bolzonella, R. Dux, M. J. Mansinen, R. Budny, P. Dumortier, M. von Hellermann, S. Jachmich, H. R. Koslowski *et al.*, “Role of sawtooth in avoiding impurity accumulation and maintaining good confinement in JET radiative mantle discharges,” *Nucl. Fusion* **43**(10), 1204 (2003).
- ⁹³W. Deng, Y. Liu, Z. Cui, Y. Dong, Y. Huang, P. Zhang, P. Sun, and B. Fu, “Sawtooth activities during impurity injection by laser blow-off in HL-2A,” *Plasma Sci. Technol.* **9**(4), 411 (2007).
- ⁹⁴J. A. Wessen, B. Alper, A. W. Edwards, and R. D. Gill, “Transport in the sawtooth collapse,” *Phys. Rev. Lett.* **79**(25), 5018 (1997).
- ⁹⁵E. Strumberger, S. Günter, E. Schwarz, C. Tichmann, and the ASDEX Upgrade Team, “Fast particle losses due to NTMs and magnetic field ripple,” *New J. Phys.* **10**, 023017 (2008).
- ⁹⁶M. García-Muñoz, H.-U. Fahrbach, S. D. Pinches, V. Bobkov, M. Brüdgam, M. Gobbin, S. Günter, V. Iguchine, P. Lauber, M. J. Mansinen *et al.*, “MHD induced fast-ion losses on ASDEX Upgrade,” *Nucl. Fusion* **49**(8), 085014 (2009).
- ⁹⁷T. Kurki-Suonio, O. Asunta, E. Hirvijoki, T. Koskela, A. Snicker, T. Hauff, F. Jenko, E. Poli, and S. Sipilä, “Fast ion power loads on ITER first wall structures in the presence of NTMs and microturbulence,” *Nucl. Fusion* **51**(8), 083041 (2011).
- ⁹⁸R. J. Buttery, “Multimachine extrapolation of neoclassical tearing mode physics to ITER,” in 22nd International Conference on Fusion Energy, Geneva, Switzerland, 2008.
- ⁹⁹S. R. Takahashi, D. P. Brennan, and C. C. Kim, “Kinetic effects of energetic particles on resistive MHD stability,” *Phys. Rev. Lett.* **102**(13), 135001 (2009).
- ¹⁰⁰D. P. Brennan, C. C. Kim, and R. J. La Haye, “Energetic particle effects on $n = 1$ resistive MHD instabilities in a DIII-D hybrid discharge,” *Nucl. Fusion* **52**(3), 033004 (2012).
- ¹⁰¹H. Cai and G. Fu, “Hybrid simulation of energetic particle effects on tearing modes in tokamak plasmas,” *Phys. Plasmas* **19**(7), 072506 (2012).
- ¹⁰²A. Polevoi, in 19th International Conference on Fusion Energy, Lyon, 2002.
- ¹⁰³M. Shimada, D. J. Campbell, V. Mukhovatov, M. Fujiwara, N. Kirneva, K. Lackner, M. Nagami, V. D. Pustovitov, N. N. Uckan, J. Wesley *et al.*, “ITER Physics Basis,” *Nucl. Fusion* **47**(6), S1 (2007).
- ¹⁰⁴H. Zohm, G. Ganstenbein, A. Isayama, A. Keller, R. J. La Haye, M. Maraschek, A. Mück, K. Nagasaki, S. D. Pinches, and E. J. Strait, “MHD limits to tokamak operation and their control,” *Plasma Phys. Controlled Fusion* **45**(12A), A163 (2003).
- ¹⁰⁵E. J. Strait, T. S. Taylor, A. D. Turnbull, J. R. Ferron, L. L. Lao, B. Rice, O. Sauter, S. J. Thompson, and D. Wróblewski, “Wall stabilization of high beta tokamak discharges in DIII-D,” *Phys. Rev. Lett.* **74**(13), 2483 (1995).
- ¹⁰⁶T. C. Hender, H. Reimerdes, M. S. Chu, A. M. Garofalo, M. P. Gryaznevich, D. F. Howell, R. J. La Haye, Y. Q. Liu, M. Okabayashi, S. D. Pinches *et al.*, “Prediction of rotational stabilisation of resistive wall modes in ITER,” in 21st IAEA Fusion Energy Conference, Chengdu, China, 2006.
- ¹⁰⁷S. A. Sabbagh, A. C. Sontag, J. M. Bialek, D. A. Gates, A. H. Glasser, J. E. Menard, W. Zhu, M. G. Bell, R. E. Bell, A. Bondeson *et al.*, “Resistive wall stabilized operation in rotating high beta NSTX plasmas,” *Nucl. Fusion* **46**(5), 635 (2006).
- ¹⁰⁸A. M. Garofalo, A. D. Turnbull, M. E. Austin, J. Bialek, M. S. Chu, K. J. Comer, E. D. Fredrickson, R. J. Groebner, R. J. La Haye, L. L. Lao *et al.*, “Direct observation of the resistive wall mode in a tokamak and its interaction with plasma rotation,” *Phys. Rev. Lett.* **82**(19), 3811 (1999).
- ¹⁰⁹R. J. La Haye, A. Bondeson, M. S. Chu, A. M. Garofalo, Y. Q. Liu, G. A. Navratil, M. Okabayashi, H. Reimerdes, and E. J. Strait, “Scaling of the critical plasma rotation for stabilization of the $n = 1$ resistive wall mode (ideal kink) in the DIII-D tokamak,” *Nucl. Fusion* **44**(11), 1197 (2004).
- ¹¹⁰A. C. Sontag, S. A. Sabbagh, W. Zhu, J. M. Bialek, J. E. Menard, D. A. Gates, A. H. Glasser, R. E. Bell, B. P. LeBlanc, M. G. Bell *et al.*, “Resistive wall mode stabilization of high- β plasmas in the National Spherical Torus Experiment,” *Phys. Plasmas* **12**(5), 056112 (2005).
- ¹¹¹H. Reimerdes, T. C. Hender, S. A. Sabbagh, J. M. Bialek, M. S. Chu, A. M. Garofalo, M. P. Gryaznevich, D. F. Howell, G. L. Jackson, R. J. La Haye *et al.*, “Cross-machine comparison of resonant field amplification and resistive wall mode stabilization by plasma rotation,” *Phys. Plasmas* **13**(5), 056107 (2006).
- ¹¹²H. Reimerdes, A. M. Garofalo, G. L. Jackson, M. Okabayashi, E. J. Strait, M. S. Chu, Y. In, R. J. La Haye, M. J. Lanctot, Y. Q. Liu, G. A. Navratil, W. M. Solomon, H. Takahashi, and R. J. Groebner, “Reduced critical rotation for resistive-wall mode stabilization in a near-axisymmetric configuration,” *Phys. Rev. Lett.* **98**(5), 055001 (2007).
- ¹¹³S. A. Sabbagh, J. W. Berkery, R. E. Bell, J. M. Bialek, S. P. Gerhardt, J. E. Menard, R. Betti, D. A. Gates, B. Hu, O. N. Katsuro-Hopkins *et al.*,

- "Advances in global MHD mode stabilization research on NSTX," *Nucl. Fusion* **50**(2), 025020 (2010).
- ¹¹⁴A. Bondeson and D. J. Ward, "Stabilization of external modes in tokamaks by resistive walls and plasma rotation," *Phys. Rev. Lett.* **72**(17), 2709 (1994).
- ¹¹⁵M. S. Chu, J. M. Greene, T. H. Jensen, R. L. Miller, A. Bondeson, R. W. Johnson, and M. E. Mauel, "Effect of toroidal plasma flow and flow shear on global magnetohydrodynamic MHD modes," *Phys. Plasmas* **2**(6), 2236 (1995).
- ¹¹⁶B. Hu, R. Betti, and J. Manickam, "Application of the low-frequency energy principle to wall modes," *Phys. Plasmas* **12**(5), 057301 (2005).
- ¹¹⁷B. Hu and R. Betti, "Resistive wall mode in collisionless quasistationary plasmas," *Phys. Rev. Lett.* **93**(10), 105002 (2004).
- ¹¹⁸I. T. Chapman, C. G. Gimblett, M. P. Gryaznevich, T. C. Hender, D. F. Howell, Y. Q. Liu, S. D. Pinches, and JET EFDA Contributors, "Stability of the resistive wall mode in JET," *Plasma Phys. Controlled Fusion* **51**(5), 055015 (2009).
- ¹¹⁹Y. Q. Liu, M. S. Chu, I. T. Chapman, and T. C. Hender, "Toroidal self-consistent modeling of drift kinetic effects on the resistive wall mode," *Phys. Plasmas* **15**(11), 112503 (2008).
- ¹²⁰J. W. Berkery, S. A. Sabbagh, R. Betti, B. Hu, R. E. Bell, S. P. Gerhardt, J. Manickam, and K. Tritz, "Resistive wall mode instability at intermediate plasma rotation," *Phys. Rev. Lett.* **104**(3), 035003 (2010).
- ¹²¹Y. Q. Liu, "Effects of α particles on the resistive wall mode stability in ITER," *Nucl. Fusion* **50**(9), 095008 (2010).
- ¹²²J. W. Berkery, S. A. Sabbagh, H. Reimerdes, R. Betti, B. Hu, R. E. Bell, S. P. Gerhardt, J. Manickam, and M. Podestà, "The role of kinetic effects, including plasma rotation and energetic particles, in resistive wall mode stability," *Phys. Plasmas* **17**(8), 082504 (2010).
- ¹²³I. T. Chapman, W. A. Cooper, J. P. Graves, M. P. Gryaznevich, R. J. Hastie, T. C. Hender, D. F. Howell, M.-D. Hua, G. T. A. Huysmans, D. L. Keeling *et al.*, "Macroscopic stability of high β MAST plasmas," *Nucl. Fusion* **51**(7), 073040 (2011).
- ¹²⁴H. Reimerdes, J. W. Berkery, M. J. Lanctot, A. M. Garofalo, J. M. Hanson, Y. In, M. Okabayashi, S. A. Sabbagh, and E. J. Strait, "Evidence for the importance of trapped particle resonances for resistive wall mode stability in high beta tokamak plasmas," *Phys. Rev. Lett.* **106**(21), 215002 (2011).
- ¹²⁵Y. Q. Liu, M. S. Chu, I. T. Chapman, and T. C. Hender, "Modelling resistive wall modes in ITER with self-consistent inclusion of drift kinetic resonances," *Nucl. Fusion* **49**(3), 035004 (2009).
- ¹²⁶L. J. Zheng, M. T. Kotschenreuther, and J. W. Van Dam, "Kinetic analysis of the resistive wall modes in the ITER advanced tokamak scenario," *Nucl. Fusion* **49**(7), 075021 (2009).
- ¹²⁷I. T. Chapman, M. P. Gryaznevich, D. F. Howell, Y. Q. Liu, and the MAST Team, "The effect of energetic particles on resistive wall mode stability in MAST," *Plasma Phys. Controlled Fusion* **53**(6), 065022 (2011).
- ¹²⁸I. T. Chapman, Y. Q. Liu, O. Asunta, J. P. Graves, T. Johnson, and M. Jucker, "Kinetic damping of resistive wall modes in ITER," *Phys. Plasmas* **19**(5), 052502 (2012).
- ¹²⁹T. Casper and A. Polevoi, private communication (2010).
- ¹³⁰A. R. Raffray, B. Calcagno, P. Chappuis, Z. Fu, A. Furmanek, C. Jiming, D.-H. Kim, S. Khomiakov, A. Labusov, A. Martin *et al.*, "The ITER blanket system design challenge," *Nucl. Fusion* **54**(3), 033004 (2014).
- ¹³¹L. Giancarli, M. Abdou, D. J. Campbell, V. A. Chuyanov, M. Y. Ahn, M. Enoeda, C. Pan, Y. Poitevin, E. Rajendra Kumar, I. Ricapito *et al.*, "Overview of the TBM Program," *Fusion Eng. Des.* **87**(5–6), 395–402 (2012).
- ¹³²V. Amoskov, "Toroidal field ripple optimization of distribution of ferromagnetic inserts," private communication (2009).
- ¹³³T. E. Stringer, "Effect of the magnetic field ripple on diffusion in Tokamaks," *Nucl. Fusion* **12**(6), 689 (1972).
- ¹³⁴R. J. Goldston, R. B. White, and A. H. Boozer, "Confinement of high-energy trapped particles in tokamaks," *Phys. Rev. Lett.* **47**(9), 647 (1981).
- ¹³⁵V. Ya. Goloborod'ko, Ya. I. Kolesnichenko, and V. A. Yavorskij, "Alpha particle transport processes in tokamaks," *Phys. Scr.* **46**, T16 (1987).
- ¹³⁶W. W. Heidbrink and G. J. Sadler, "The behaviour of fast ions in tokamak experiments," *Nucl. Fusion* **34**(4), 535 (1994).
- ¹³⁷K. Shinohara, H. Kawashima, K. Tsuzuki, K. Urata, M. Sato, H. Ogawa, K. Kamiya, H. Sasao, H. K. S. Kimura *et al.*, "Effects of complex magnetic ripple on fast ions in JFT-2M ferritic insert experiments," *Nucl. Fusion* **43**(7), 586 (2003).
- ¹³⁸K. Shinohara, S. Sakurai, M. Ishikawa, K. Tsuzuki, Y. Suzuki, K. Masaki, O. Naito, K. Kurihara, T. Suzuki, Y. Koide *et al.*, "Ferritic insertion for reduction of toroidal magnetic field ripple on JT-60U," *Nucl. Fusion* **47**(8), 997 (2007).
- ¹³⁹G. J. Kramer, A. McLean, N. Brooks, R. V. Budny, X. Chen, W. W. Heidbrink, T. Kurki-Suonio, R. Nazikian, T. Koskela, M. J. Schaffer *et al.*, "Simulation of localized fast-ion heat loads in test blanket module simulation experiments on DIII-D," *Nucl. Fusion* **53**(12), 123018 (2013).
- ¹⁴⁰K. Tani, M. Azumi, H. Kishimoto, and S. Tamura, "Effect of toroidal field ripple on fast ion behavior in a tokamak," *J. Phys. Soc. Jpn.* **50**(5), 1726 (1981).
- ¹⁴¹J. A. Heikkilä and S. K. Sipilä, "Power transfer and current generation of fast ions with large- $k\theta$ waves in tokamak plasmas," *Phys. Plasmas* **2**(10), 3724 (1995).
- ¹⁴²G. J. Kramer, R. V. Budny, A. Bortolon, E. D. Fredrickson, G. Y. Fu, W. W. Heidbrink, R. Nazikian, E. Valeo, and M. A. Van Zeeland, "A description of the full-particle-orbit-following SPIRAL code for simulating fast-ion experiments in tokamaks," *Plasma Phys. Controlled Fusion* **55**(2), 025013 (2013).
- ¹⁴³K. Shinohara, "Simulations of toroidal field ripple and tbm effects on energetic particle losses in ITER," private communication (2010).
- ¹⁴⁴K. Shinohara, T. Kurki-Suonio, D. Spong, O. Asunta, K. Tani, E. Strumberger, S. Briguglio, T. Koskela, G. Vlad, S. Günter *et al.*, "Effects of complex symmetry-breakings on alpha particle power loads on first wall structures and equilibrium in ITER," *Nucl. Fusion* **51**(6), 063028 (2011).
- ¹⁴⁵K. Shinohara, K. Tani, T. Oikawa, S. Putvinski, M. Schaffer, and A. Loarte, "Effects of rippled fields due to ferritic inserts and ELM mitigation coils on energetic ion losses in a 15 MA inductive scenario in ITER," *Nucl. Fusion* **52**(9), 094008 (2012).
- ¹⁴⁶K. Tani, K. Shinohara, T. Oikawa, H. Tsutsui, S. Miyamoto, Y. Kusama, and T. Sugie, "Effects of ELM mitigation coils on energetic particle confinement in ITER steady-state operation," *Nucl. Fusion* **52**(1), 013012 (2012).
- ¹⁴⁷M. A. Van Zeeland, N. M. Ferraro, W. W. Heidbrink, G. J. Kramer, D. C. Pace, X. Chen, T. E. Evans, R. K. Fisher, M. García-Muñoz, and J. M. Hanson, "Modulation of prompt fast-ion loss by applied $n=2$ fields in the DIII-D tokamak," *Plasma Phys. Controlled Fusion* **56**(1), 015009 (2014).
- ¹⁴⁸T. Oikawa, "Assessment of fast ion losses due to ELM control coils including plasma response effects," private communication, Oxford, UK (2013).
- ¹⁴⁹O. Schmitz, M. Becoulet, P. Cahyna, T. Evans, Y. Feng, H. Frerichs, D. Harting, A. Kirschner, A. Kukushkin, and R. E. Laengner, "Three-dimensional fluid modeling of plasma edge transport and divertor fluxes during RMP ELM control at ITER," in 24th IAEA Fusion Energy Conference, San Diego, CA, USA, 2012.
- ¹⁵⁰E. Strumberger, S. Günter, P. Merkel, E. Schwarz, and C. Tichmann, "Self-consistent three-dimensional computations of non-axisymmetric ITER equilibria," *Nucl. Fusion* **50**(2), 025008 (2010).
- ¹⁵¹M. Bruno, Y. Nakamura, Y. Suzuki, K. Shinohara, G. Matsunaga, and K. Tani, "The finite beta effects on the toroidal field ripple in a tokamak plasma," *Plasma Sci. Technol.* **15**(2), 115 (2013).